Finite Element Modeling of Steel Corrosion in Concrete Structures

Mehrnoush Farhadi

Thesis submitted to the faculty of the Virginia Polytechnic Institute and State University
in partial fulfillment of the requirements for the degree of

Master of Science
In
Civil Engineering

Ioannis Koutromanos, Chair
Carin L. Roberts-Wollmann, Member
Matthew H. Hebdon, Member

July 10, 2018
Blacksburg, VA

Keywords:
Advection-diffusion, Anode and Cathode, Chloride-induced Corrosion, Chloride transport, Electro-chemical cell, Finite element analysis, Moisture isotherm, Moisture transport analysis, Nonlinear analysis, Reinforced concrete structures, Relative humidity, Polarization, SUPG method, Tafel diagram, Temperature, Thermal analysis

Finite Element Modeling of Steel Corrosion in Concrete Structures

Mehrnoush Farhadi

ABSTRACT

Concrete is a popular construction material for bridges, due to its high durability and energy efficiency. An important concern for concrete bridges is the possible occurrence of chloride- induced corrosion in prestressing strands and reinforcing bars, which may substantially impact the service life of such structures. Chloride- induced corrosion is a complicated electrochemical process which is affected by heat transfer, moisture flow and transport of chemical species through the concrete pore network. Reliable and robust analytical tools are required to allow multi-physics simulations of steel corrosion.

This study has developed a nonlinear finite element analysis program, called *VT-MultiPhys*, to enable multi-physics simulations, including analyses of chloride-induced corrosion. The program includes constitutive laws, element formulations and global solution schemes to allow the analysis of steady-state (static) and time-dependent (dynamic) problems, involving multiple, coupled processes such as mechanical deformation, heat transfer, mass flow and chemical reactions combined with advective/diffusive transport of the various species. Special analysis schemes, based on the streamline-upwind Petrov-Galerkin (SUPG) method, have also been implemented to address the spatial instabilities which characterize analyses of advection-dominated transport.

The finite element modeling scheme, constitutive laws and boundary conditions for analysis of chloride-induced corrosion are described in detail. The constitutive laws can be combined with inelastic material models to capture the damage (e.g., cracking) due to chloride-induced corrosion. A set of verification analyses is presented, to demonstrate the capabilities of *VT-MultiPhys* to conduct different types of simulations and reproduce the closed-form analytical solutions of simple cases. Validation analyses for heat conduction, moisture flow and chloride transport, using data from experimental tests in the literature, are also presented.

Finite Element Modeling of Steel Corrosion in Concrete Structures

Mehrnoush Farhadi

GENERAL AUDIENCE ABSTRACT

The deterioration of concrete structures and infrastructures due to the chloride-induced corrosion in prestressing strands and reinforcing bars may substantially impact the service life of such structures. Chloride-induced corrosion is a complicated electrochemical process which is initiated and proceeds due to the chloride attacks at the surfaces of concrete structures and ends in the volume expansion, cracking and spalling of concrete. Due to the lack of comprehensive modeling tool, which can simultaneously comprise the influential factors in chloride-induced corrosion, the realistic estimation of the service life of reinforced concrete structures is still challenging. Reliable and robust analytical tools are required to allow multi-physics simulations of steel corrosion.

This study has developed a comprehensive finite element analysis program, called *VT-MultiPhys*, for calculating and monitoring the contribution of chloride ions to chloride-induced corrosion during service life of concrete structures. The present analysis program enables modeling of the coupled physical process including heat transfer, moisture flow and transport of chemical species through the concrete pore network. Also, by modeling the influence of flexural cracks on chloride transport in concrete, the analysis program is able to predict the rate of steel corrosion in cracked concrete structures.

A set of verification analyses is presented, to demonstrate the capabilities of *VT-MultiPhys* to conduct different types of simulations of heat conduction, moisture flow and chloride transport and the comparison is found to be satisfactory. The element formulations and solution algorithms in *VT-MultiPhys* also allow the investigation of other long-term deterioration mechanisms, such as carbonation-induced corrosion, alkali-silika reaction (ASR) and sulfate attack. The present contribution will hopefully enable and facilitate future research in these topics, through the formulation and implementation of proper constitutive laws and chemical reaction equations.

To my family

Acknowledgements

I would like to express my gratitude to the Civil and Environmental Engineering department of Virginia Tech for supporting my research through a graduate research assistantship.

I would like to sincerely express my deepest gratitude and special thanks to my adviser, Professor Ioannis Koutromanos, for providing guidance throughout this research. I also appreciate his patience and constructive criticism.

Further acknowledgements are due to the members of my thesis committee, namely, Professor Carin Roberts-Wollmann, and Professor Matthew Hebdon for providing useful feedback during the progress of this research.

I would also like to thank Professor Maryam Shakiba and Dr. David Mokarem for providing useful help and suggestions on several aspects of my work.

Additionally, I would like to thank Alireza Farzampour and Adrian Tola Tola for their technical support and helpful suggestions. Special thanks are due to my friend, Setareh Ghaychi Afrouz, for both her technical and emotional support that facilitated my work.

Finally, I am grateful for the love, encouragement, and tolerance of my husband, Siavash, who has made all the difference in my life. Without his patience and love, I could not have completed this thesis. A special word of thanks goes to my parents, Ahmad Reza

and Sholeh, and my beloved sisters Farnoush and Arshin, who always support me spiritually throughout my life.

Table of contents

List of Figures

List of Tables

List of Abbreviations

BSB	: Brunauer- Skalny- Bodor
BSF	: Blast Furnace Slag
C-S-H	: Calcium-Silicate-Hydrate (C-S-H) gel
FA	: Fly Ash
OPC	: Ordinary Portland Cement
p.H	: Potential Hydrogen
SUPG	: Streamline-Upwind Petrov-Galerkin
VT- MultiPhys	: Virginia Tech- Multiphysics program

Preface

This thesis report contains a total of seven chapters.

Chapter 1 constitutes an introduction, with a brief explanation of the definition and consequence of chloride-induced corrosion of steel bars in concrete structures, and the essence of computational finite element tools to quantitatively simulate this multiphysics phenomenon. Also, chapter 1 describes the finite element program, *VT-Multiphys* that was created in this study to enable simulation of multi-physics processes, including chloride-induced corrosion in reinforced and prestressed concrete. The overview of solution schemes to describe heat transfer, moisture transport and chloride transport in concrete are presented.

Chapter 2 presents the theoretical background and literature review pertaining to heat, moisture and chloride transport and steel corrosion in concrete structures. A survey of literature related to simulation of chloride-induced corrosion in concrete structures is also provided in the specific chapter.

Chapters 3, 4 and 5 present methodology and verification analyses of heat transfer, moisture transport and transport of chloride in concrete, using data from experimental tests. Guidelines for the calibration of the proposed analytical models are also provided.

Chapter 6 present methodology and analyses of coupled advection-diffusion transport of chemical substances such as chloride ions in concrete. The effect of crack and mesh

refinement on the advective and diffusive transport of chloride are discussed in this chapter.

Chapter 7 provides a summary of the present study, presents the main conclusions of this work and provides recommendations for future research.

1 Introduction

Reinforced concrete is a popular construction material for bridges due to its high durability and affordability. A significant concern for concrete bridges is the possible occurrence of chloride-induced corrosion in prestressing strands and steel bars, which may substantially impact the service life of such structures.

Chloride-induced corrosion is initiated and proceeds due to the chloride attacks at the surfaces of concrete structures. Chloride ions penetrate from concrete surfaces into the steel bars in concrete structures. The accumulation of chloride ions around steel bars lead to deterioration of the protective passive layer that is initially formed in the vicinity of steel bars. Also, the chloride ions intrigue the electrochemical reactions in concrete and so they contribute to the corrosion process in concrete.

Chloride-induced corrosion contributes to the volume expansion, increasing tensile stresses, cracking and spalling of concrete, reduction of the cross sectional area of steel bars and weakening of the bond between concrete and steel (Zhou et al. 2015). Figure 1.1 schematically illustrates some types of major failures due to the chloride-induced corrosion of steel in concrete bridges. The damaged parts of steel and concrete should be repaired or replaced to prevent further corrosion process in concrete structures. There are several different repair strategies, such as deck sealers, patching of the concrete bridge decks, deck overlays, rehabilitation and replacement. These methods can be applied based

on the depth of corrosion and the level of damage to improve the system performance and increase the concrete service life. In the United States, the repair of damage in concrete bridge decks and their components due to chloride-induced corrosion costs roughly 100 to 300 million US dollars per year (Zhou et al. 2015). Therefore, it is of significant importance to develop an advanced predictive tool to monitor the rate of steel corrosion during the service life of concrete structures.

Figure 1.1: Concrete failures due to chloride-induced corrosion of steel in concrete, (a) corrosion of bridge pier and piles due to sea salt attack ((Moser et al, 2011), (b) bridge piling failure (NACE, 2014), (c) spalling of reinforced concrete pier (cpt, 2017), (d) delamination and spalling of the Gardiner Expressway's concrete in Toronto, Canada (Fahim, Giatech, 2018)

Chloride-induced corrosion in concrete is a multi-physics phenomenon that is affected by environmental exposure conditions such as the ambient temperature, humidity and

chloride transport across the surface of concrete structure. There are several empirical and numerical studies about the causes and impacts of steel corrosion in concrete. These studies proposed practical techniques to measure and evaluate the corrosion damages in concrete structures (Dao et al. 2010, Ghods et al. 2008, Hansen and Saouma 1999, Isgor and Ghani Razaqpur 2006, Kulakowski et al. 2009, Pour-Ghaz et al. 2009, Wong et al. 2010).

A porous concrete medium consists of various types of materials, including cement, additives, water and aggregates. Several parameters affect the chloride-induced corrosion of steel bars in concrete structures. In spite of the significant progress in numerical modeling and nonlinear finite element methods, the complexity of concrete environment and the coupling effects of different substances on each other make it difficult for researchers to accurately simulate all the influential parameters and their interactions.

Also, most of these methods may have limited validity, as they commonly neglect the effect of environmental conditions on corrosion. Therefore, it is important to develop an applicable and comprehensive tool to simulate the real physical behavior of reinforced concrete systems, surface boundaries of concrete and influential environmental exposure conditions.

1.1 Objective and scope of thesis

Due to the lack of comprehensive modeling tool, which can simultaneously comprise the influential factors in chloride-induced corrosion, the realistic estimation of the service

life of reinforced concrete structures is still challenging. This thesis aims to develop a finite element tool to simulate the coupled physical process in concrete structures due to chloride-induced corrosion. Also, the contribution of chloride ions to chloride-induced corrosion is the key factor that should be calculated and monitored during service life of concrete structures.

The developed nonlinear, multi-physics finite element program, called *VT-MultiPhys*, is able to model the chloride transport in concrete as the multi-physics problem which is influenced by the ambient parameters including temperature and relative humidity. Also, the analysis program models the chemical reactions in concrete medium such as carbonation reaction and the mechanical deformation and damage in concrete.

As shown in Figure 1.2, a concrete member has a multi-faceted interaction with its surroundings. The interaction includes exchange of heat, moisture and chemical species such as chloride ions. The newly developed program can model this interaction by means of appropriate, generalized natural boundary conditions.

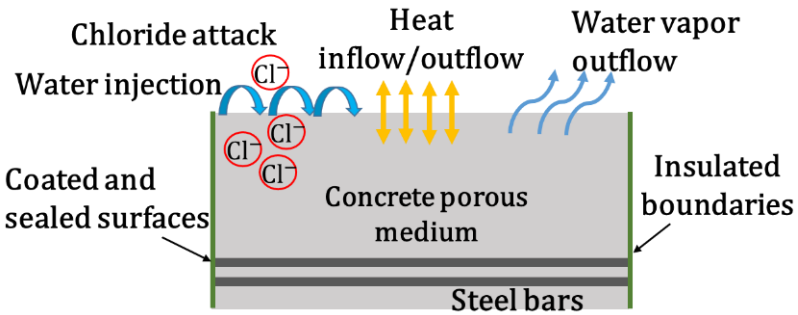

Figure 1.2: Schematic illustration of the interaction of concrete structure with it's surrounding environment

The various processes (heat conduction, moisture transport, transport of chemical species such as chloride ions) are coupled among them. The coupling is assumed to be one-way: the temperature (associated with heat conduction) affects both moisture and chemical species transport, and moisture flow contributes (through advection) to the transfer of chemical species. The impact of moisture and chemical species transport on heat conduction is neglected in the present study.

The analysis scheme for heat conduction, moisture flow and chemical transport is described in the following chapters. Before this presentation, an overview of the background pertaining to various processes associated with corrosion is provided, together with a review of relevant literature.

2 Theoretical background – Literature review

2.1 Fundamentals of reinforcing steel corrosion in concrete

Steel corrosion in concrete is considered as the complex multi-physics phenomenon which is influenced by various parameters. Modeling the concrete corrosion requires consideration of several chemical substances in different physical phases; such as aggregate, cement, liquid water, water vapor, oxygen, chloride, and their interactions in concrete medium. The characteristics of concrete porous body and concrete surfaces which are exposed to the time-dependent environmental conditions, chemical and electrochemical reactions in concrete due to the chloride-induced corrosion and the coupling effects of different physical problems such as heat transfer; moisture transport and chloride transport should be accurately simulated.

According to the literature, there are only a small number of studies that have comprehensively considered these influential parameters and proposed practical computational models for steel corrosion in concrete structures. Most of the current studies introduced nonlinear finite element algorithms for modeling the electrochemical mechanism in concrete due to chloride-induced corrosion process. However, there are only a small number of articles for modeling the effect of environmental parameters on the initiation of corrosion and corrosion process during the service life of concrete structures. Furthermore, some of the current studies proposed oversimplified computational models for simulation of steel corrosion which are not able to capture the

real physical behavior of reinforced or prestressed concrete structures. The oversimplifications are based on unpractical assumptions such as considering constant value for water conductivity coefficient and chloride diffusion coefficient and constant uniform distribution of temperature and water content during life span of concrete structures.

In this chapter, the different types of corrosion are introduced and the chemistry of chloride-induced corrosion is described in detail. Afterward, the polarization effects and the different terms of polarization in electrochemical cells are thoroughly illustrated. In addition, a Tafel diagram and its application to simulate the polarization effects in concrete systems is proposed. Finally, the previous studies of modeling of the corrosion initiation and the process of corrosion are reviewed.

2.2 Steel passivity

As shown in Figure 2.1, in the presence of moisture (H_2O) and oxygen (O_2) in concrete structures, a very thin passive layer with a thickness of 1 to 10 mm is formed around steel surface bars. A passive layer protects steel bars against corrosion progress. Due to the presence of hydroxyl ions, concrete is a high alkaline medium with a pH of 11.75 to 13.5 (Hansen and Saouma, 1999b). The alkaline environment provides the ideal condition for steel to maintain its passivity. The main component of passive layer is not clearly specified. However, a thin oxide protective film in high alkaline concrete environment is formed where concrete pH exceeds13. The high alkalinity of concrete environment is due to presence of a sufficient concentration of hydroxide salts such as saturated calcium

hydroxide, sodium hydroxide, potassium hydroxide or a combination of some or all of them (Moreno et al. 2004).

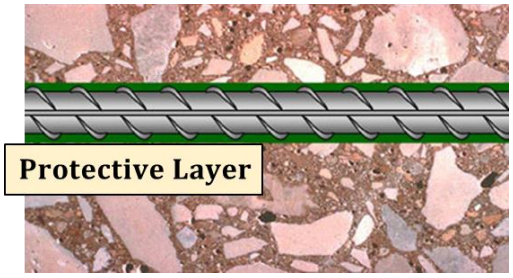

Figure 2.1: Passive layer around reinforcing steel bars in concrete (PCA 2017)

The hydroxyl ions in passive layer tend to chemically react with the corrosive agents including chloride ions or other chemical salts accumulate around the steel bars. Due to the consumption of hydroxyl ions, the pH of concrete body is reduced and causes weakening of passive layer. Any other factors which increase the risk of steel exposure to aggressive environmental attacks such as increase in CO_2 concentration and carbonation reaction in concrete adversely impacts the alkalinity of concrete environment. The characteristics of concrete body, external boundaries, surface cracks and crack propagation, chemical properties of steel bars and the mechanical properties of reinforced concrete also negatively affect alkalinity. Depassivation is referred to as the partial or complete loss of passive layers around steel bars in concrete due to the significant drop in pH of concrete medium. Steel corrosion initiates and progressively increase in concrete immediately after depassivation (Gouda 1970, Uhlig and Revie 1985).

2.3 Different types of corrosion

Concrete is an anisotropic and inhomogeneous material consists of different phases and substances. Due to the complexity of concrete pore structures, there is a heterogeneous distribution of water, oxygen, chloride ion or other salts, which causes characteristic differences in concrete environment. In the presence of sufficient water, oxygen and chemical salts around steel bars in concrete, passive layer breaks down and loses its resistance to corrosion. Depassivation occurs due to an excessive chloride concentration or the penetration of atmospheric CO_2 in concrete. The steel corrosion in concrete is categorized as chloride-induced corrosion and carbonation-induced corrosion based on the reason which causes depassivation.

2.3.1 Chloride-induced corrosion

Chloride-induced corrosion is common in marine structures and concrete structures which are exposed to de-icing salts such as bridge decks. In Figure 2.2, the initiation of chloride-induced corrosion in reinforced concrete structures which is exposed to chloride attack is schematically explained. Montemor et al. (2003) figured out that in the presence of sufficient water, oxygen and chloride ions, steel corrosion initiates due to the destruction of protective layer. Chloride ions have the most contribution to the initiation and process of chloride-induced corrosion in concrete.

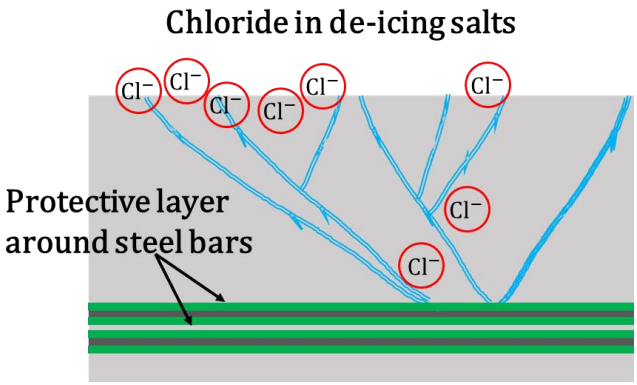

Figure 2.2: Schematic illustration of chloride penetration to concrete system which is exposed to de-icing salts

The initiation stage of corrosion is referred as to the part of service life of concrete systems before depassivation occurs. The chloride-induced corrosion initiates when chloride concentration, C_{Cl}, exceeds the threshold value. Castel et al. (2000) and Alhozaimy et al. (2012) verified the effect of various factors on the amount of chloride diffusion in concrete including concrete cover thickness, water to cement ratio, cement type and admixture, ambient temperature and relative humidity. Li et al. (2011) performed several experimental tests to study the effects of concrete characteristics, stress distribution and environmental conditions on the rate of chloride-induced corrosion. They concluded that decreasing the water to cement ratio (w/c), improves the resistance of concrete to chloride attack. In general, chloride transport in concrete depends on the time-dependent distributions of temperature, relative humidity and tensile stress of a concrete system (Doa et al. 2010 a and b, Hansen and Saoumo 1999 a and b, Isgor and Ghani Razaqpur 2006, Maekawa et al. 2009, Michel et al. 2013, Pour-Ghaz et al. 2009).

2.3.2 Carbonation-induced corrosion

If atmospheric CO_2 penetrates into concrete systems, CO_2 can combine with calcium hydroxide in concrete wherever oxygen and water is sufficient. As shown in Figure 2.3, carbonation is the chemical reaction which occurs around steel bars in concrete, as follows:

$$Ca^{2+}(aq) + 2OH^{-}(aq) + 2H^{2+}(aq) + CO_3^{2-}(aq) \rightarrow CaCo_3(s) + 2H_2O \qquad (2\text{-}1)$$

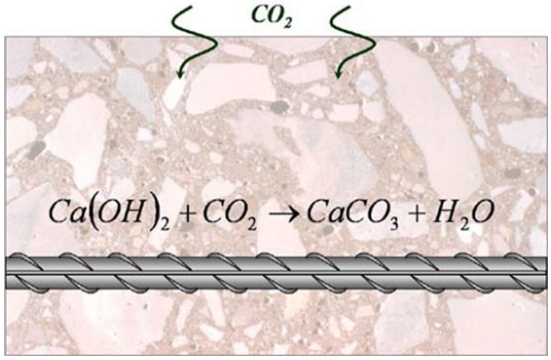

Figure 2.3: Carbonation reaction due to the diffusion of CO2 into concrete systems (PCA, 2017)

The concrete pH depends on the time-dependent distribution of hydroxyl ions in concrete body. Due to the consumption of hydroxyl ions in carbonation reaction, concrete pH may be significantly reduced. Consequently, the protective layer depassivates if the concrete pH in vicinity of steel bars drops to 8 (Zhou et al. 2015). Recently, the high rate of released CO_2 as the result of air pollution, escalates the carbonation induced corrosion rate in concrete structures. Therefore, understanding the corrosion process is matter of concern for recent civil engineering studies as the structures are more exposed to CO_2. Das et al. (2012) verified the influential parameters on carbonation-induced corrosion

including water to cement ratio, age of concrete, curing condition, cover thickness, supplementary cementitious materials (e.g., pozzolanic materials), oxygen penetration, carbonation resistivity and ambient conditions at concrete boundary surfaces (Yoon et al. 2007, Marques and Costa 2009). In general, improve in the surface characteristic and properties of mixed materials leads to the increase in concrete resistivity to the aggressive environmental agents (Kulakowski et al. 2009, Isgor and Ghani Razaqpur 2006).

2.3.3 Coupled chloride-induced and carbonation-induced corrosion

If CO_2 penetrates into concrete body and moves toward steel bars, the concrete medium is at the risk of both chloride-induced and carbonation-induced corrosion. Carbonation reaction leads to increasing the water content and also reducing the concrete porosity. Due to the concrete porosity reduction, the diffusion of aggressive environmental agents may decrease. However, the volume expansion due to the carbonation reactions increases internal stresses and influences the crack propagation of concrete. Consequentially, carbonation reactions in a concrete medium causes the raise in chloride transport through the cracks and openings of the concrete body. Furthermore, due to the consumption of hydroxyl ions during the carbonation reactions, concrete pH along steel bars reduces. Therefore, in less alkaline environment, the protective layer of steel bars may be deteriorated even in exposure to the lower chloride concentration along steel bars (Isgor 2006, Papadakis et al. 1991).

The expansive products that are formed in the interface of concrete and steel bars due to the coupled chloride-induced and carbonation-induced corrosion increase the internal

stresses of the concrete in vicinity of steel bars. The increase in concrete tensile stress results in the crack propagation and spalling of concrete. The other consequence of coupled chloride-induced and carbonation-induced corrosion is diminishing the thickness of steel bars and reducing its load and elongation capacity. In presence of sufficient water and oxygen along steel bars in concrete, carbonation-induce corrosion uniformly proceeds along steel bars. However, chloride-induced corrosion can be locally distributed where the accumulation of chloride ions at surface of steel bar exceeds the threshold value (Isgor and Ghani Razaqpur 2006).

Saetta and Vitaliani (2004) evaluated 54 experimental cases considering the effects of water to cement ratio (w/c), exposure conditions and the time-transient profile of chloride ions and CO_2 on steel corrosion in concrete. They concluded that in both types of chloride-induced and carbonation induced corrosion, accumulation of corrosive agents along steel bars in concrete is the main factor of depassivation. In addition, they concluded that compare to the chloride-induced corrosion, the rate of corrosion progress is slower in carbonation-induced corrosion in concrete. Also, chloride-induced corrosion causes more complicated damage in concrete structures, which increases the financial burden of repairmen and maintenance of concrete structures (Zhou et al. 2015, Miyazato and Otsuki 2010, Ye et al. 2013).

2.4 Different stages of corrosion

Hansen and Saouma (1999 a) categorized the process of steel corrosion during the service life of concrete structures by three stages of initiation, propagation and

deterioration. The initiation stage corresponds to the part of service life when concrete is exposed to corrosive environmental factors, such as chloride ions and CO_2 penetration. Concrete pH reduces and depassivation is triggered at the initiation stage of corrosion. The second stage or the propagation stage begins immediately after partial or complete loss of the passive layer due to the depassivation of protective layer. This propagation stage ends with the deterioration stage at the end of life span when concrete structures are out of serviceability due to the failure or fracture.

The spatial distribution of hydroxyl ions in concrete is the key factor to predict the initiation of corrosion and corrosion process. Several experimental and numerical studies verified the effect of hydroxyl ions on chloride transport in concrete, CO_2 diffusion and pH changes in the reinforced concrete structures (Isgor and Ghani Razaqpur 2006, Maekawa et al. 2009, Michel et al. 2013). According to the studies, hydroxyl ion as the chemical reactant which is consumed during the corrosion process contribute to the both chloride-induced corrosion and carbonation-induced corrosion. In the coupled chloride-induced and carbonation-induced corrosion, the hydroxyl ion concentration in concrete body is significantly reduced due to the consumption in chemical reaction which ends to the reduction in concrete pH along steel bars. It is still challenging to define the threshold value for hydroxyl ion concentration along steel bars in concrete in the coupled chloride-induced and carbonation-induced corrosion (Papadakis et al. 1991, Saetta et al. 1993, Martin-Perez et al. 2001, Samson and Marchand 2003, Thomas and Bamforth 1999, Isgor and Razaqpur 2004). Despite the wide range of studies about corrosion, only a small number of them simultaneously modeled the coupling effects of the initiation of corrosion

and corrosion process (Hansen and Victor E. Saouma 1999, Silva 2013, Tuutti 1982, Pour-Ghaz 2007, Li 2002, Ji 2006), among which, Isgor and Razaqpur (2006) simulated the physical behavior of a concrete system considering the influential environmental parameters, such as temperature, relative humidity, chloride and CO_2 diffusion, oxygen and hydrogen ions diffusion and penetration of other salts in concrete. They examined the coupling effects of these parameters on the rate of corrosion. However, oversimplification of the environmental parameters at the initiation stage decreased the accuracy of their analysis.

2.5 Modeling of the influential scalar parameters

The durability and serviceability of reinforced concrete structures is severely affected by the corrosion of steel bars in concrete. The chloride-induced corrosion in concrete initiates when the chloride concentration along steel bars exceeds the threshold value. Therefore, the time- dependent distribution of chloride concentration in concrete should be monitored during the service life of concrete structures. Chloride transport in concrete is a coupling multi-physics phenomenon which depends on the environmental exposure conditions including ambient temperature and relative humidity. Consequently, chloride-induced corrosion in concrete is implicitly impacted by the physical parameters including temperature and water content in concrete.

2.5.1 Semi-discrete finite element equations for time-dependent scalar field (parabolic) problems

The influential physical parameters which affect the chloride-induced corrosion are temperature, water content and chloride concentration in concrete. These scalar field variables can be obtained by solving the parabolic equation (2-2) which includes the first partial derivative of physical field, P with respect to time (Koutromanos 2018), as follows:

$$[C]\{\dot{P}(t)\} + [K]\{P(t)\} = \{f(t)\} \tag{2-2}$$

where $P(t)$ is the time-dependent scalar field variable (e.g., temperature in thermal analysis, water content in moisture transport analysis and chloride concentration in chloride diffusion- advection analysis), $[C]$ and $[K]$ are coefficient arrays and $\{f(t)\}$ is the equivalent nodal vector. By means of a gather array, $\left[L^{(e)}\right]$ the global arrays and right-hand-side vector are obtained, as follow:

$$[C] = \sum_{e=1}^{Ne}\left[L^{(e)}\right]^{T}\left[C^{(e)}\right]\left[L^{(e)}\right] \tag{2-3}$$

$$[K] = \sum_{e=1}^{Ne}\left[L^{(e)}\right]^{T}\left[K^{(e)}\right]\left[L^{(e)}\right] \tag{2-4}$$

$$\{f\} = \sum_{e=1}^{Ne}\left[L^{(e)}\right]^{T}\left\{f^{(e)}\right\} \tag{2-5}$$

where Ne is the total number of element of a finite element model. The element arrays, $\left[K^{(e)}\right]$ and $\left[C^{(e)}\right]$ and element right-hand-side vector, $\left\{f^{(e)}\right\}$ are obtained by the following equations:

$$\left[C^{(e)}\right] = \int\int\int_{\Omega}\left[N^{(e)}\right]^{T}\left[m^{(e)}\right]\left[N^{(e)}\right]d\forall \tag{2-6}$$

$$\left[K^{(e)}\right] = \int\int\int_{\Omega}\left[B^{(e)}\right]^{T}\left[D_{P}^{(e)}\right]\left[B^{(e)}\right]d\forall \tag{2-7}$$

$$\left\{f^{(e)}\right\} = \int\int\int_{\Omega}\left[N^{(e)}\right]^{T}s^{(e)}d\forall + \int\int_{\Gamma}\left[N^{(e)}\right]^{T}.\bar{q}(t)d\Gamma \tag{2-8}$$

where $\left[D_{P}^{(e)}\right]$ is the material conductivity array for each specific problem, $\left[m^{(e)}\right]$ is the material dependent array and $\bar{q}(t)$ is the heat flux, moisture flux and chloride flux at concrete surface for thermal analysis, moisture transport analysis and chloride diffusion analysis, respectively. $\left[N^{(e)}\right]$ is the shape function array. The gradient of scalar field variable is the product of the element, $\left[B^{(e)}\right]$ and the nodal values vector. Table 2.1 presents the parameters of the influential scalar field analysis in chloride-induced corrosion in concrete.

Table 2.1: Different scalar field variables

Equation	Scalar Field Variable, P	D_P	Q	$\bar{q}$	Constitutive Law
Heat Flow	Temperature, T	Thermal Conductivity, D_T	Heat Supply	Heat Flux	Fourier: $q=-D_T\nabla T$
Moisture Transport Through Concrete Pores	Water Content, θ_w	Moisture Conductivity of Concrete, D_w	Fluid Supply	Volume Flux	Darcy: $q=-D_w\nabla w$
Chemical Ion or Substances Diffusion	Ion/Substance Concentration, [C]	Diffusion Coefficient, D_C	Ion/Substance Supply	Ion Flux	Fick: $q=-D_C\nabla C$

If the material conductivity array, $[D_P]$ is independent of the physical field variable, the material is referred as the linear material. In other words, any dependence of conductivity coefficient array, $[D_P]$ on the scalar field variable, P causes material nonlinearity. Generally, the nonlinear boundary condition is referred to the flux at boundaries which is the nonlinear function of field variable, P.

2.5.2 Modeling of heat transfer in concrete

In order to model the progress of chloride-induced corrosion of steel bars in concrete, the multi-physics analysis should simultaneously be conducted to capture the realistic figure of the coupling effects of different fields at each time step of analysis. Heat transfer

analysis is one of the most important physical parameters which affects all the other field variables including moisture transport, chemical diffusion and solid mechanic analysis. There are a small number of articles that show the dependency of thermal analysis to the other physical fields. This coupling effect may be considered by modeling the heat released or absorbed during the cement hydration or other chemical reaction s in concrete. According to Zhou (2004), a large number of parameters such as concrete resistivity, density and viscosity of concrete, thermal stress, chloride diffusion coefficient depend on temperature distribution during the service life of concrete systems. Generally, heat transfer in concrete is categorized as a time-dependent scalar field problem which is governed by the Fick's law. As shown in Table 2.1, temperature, T is the scalar field variable in thermal analysis and D_T is the thermal conductivity of concrete. The material dependent array, $\left[m^{(e)}\right]$ in thermal analysis is defined as follows:

$$\left[m^{(e)}\right] = \rho . C\ [I] \tag{2-9}$$

where ρ is concrete density (kg/m^3), C is the specific heat of concrete (J/kg °C) and $[I]$ is the unity array. The temperature dependency of material properties causes nonlinearity in heat transfer analysis. Lienemann et al. (2005) introduced a polynomial function of temperature for thermal conductivity of isotropic and homogeneous materials. As shown in equation (2-10), D_T is a nonlinear function of the temperature field where a_i are constant coefficients of polynomial function and i varies from zero to an arbitrary value of n:

$$D_T(T) = a_0 + a_1 T + \cdots + a_n T^n = \sum_{i=0}^{n} a_i T^i \tag{2-10}$$

As stated in the literature, the concrete density and capacity are defined as functions of temperature (Zhou 2004, Shin et al. 2002, Zhu and Chao 2002, Farzampour and Radlinska 2016, Farzampour 2017).

$$\rho(T) = \begin{cases} \rho_{(20℃)} & T \leq 115℃ \\ \rho_{(20℃)}\left(1 - \frac{0.02(T-115)}{85}\right) & 115℃ \leq T \leq 200℃ \\ \rho_{(20℃)}\left(0.98 - \frac{0.03(T-200)}{200}\right) & 200℃ \leq T \leq 400℃ \\ \rho_{(20℃)}\left(0.95 - \frac{0.07(T-400)}{800}\right) & 400℃ \leq T \leq 1200℃ \end{cases} \quad (2\text{-}11)$$

in which $\rho(T)\left(\frac{Kg}{m^3}\right)$ is the density of concrete at temperature T, in Celsius degrees. The specific heat, C(T) $(\frac{J}{Kg.°K})$ is also impacted by temperature, as follows:

$$C(T) = \begin{cases} 900 & T \leq 100℃ \\ 900 + (T - 100) & 100℃ \leq T \leq 200℃ \\ 1000 + (T - 200)/2 & 200℃ \leq T \leq 400℃ \\ 1100 & 400℃ \leq T \leq 1200℃ \end{cases} \quad (2\text{-}12)$$

Shin et al. (2002) introduced the temperature dependent material properties based on experimental tests, defined in equations (2-13) to (2-16).

$$\rho(T) = 0.0001896T^2 - 0.3980T + 2259.62 \quad (2\text{-}13)$$

$$D_T(T) = 13.647 - 6T^2 - 0.002569T + 2.2472 \quad (2\text{-}14)$$

$$\alpha(T) = (91.639 - 7T^2 - 0.001370T + 0.9091)10^{-6} \quad (2\text{-}15)$$

$$C(T) = \frac{K(T)}{\alpha(T).\rho(T)} \quad (2\text{-}16)$$

Also, three forms of energy transfer including convection, q_c, surface irradiation, q_r, and solar radiation or total absorbed radiation, q_s affect the time-dependent heat transfer in concrete (Hansen and Saouma, 1999a). The total heat flux, q in concrete surface boundaries is calculated as follows:

$$q_c - q_r - q_s - q = 0.0 \tag{2-17}$$

Based on the Newton's law of cooling, the heat outflow due to the convection effect is calculated by equation (2-18):

$$q_c = h_c(T(t) - T_a) \tag{2-18}$$

where T(t) is the temperature at concrete surface (℃) at time t and $T_a(t)$ is the ambient temperature in vicinity of concrete surface. The parameter h_c is the convection heat transfer film coefficient (W/m^2 ℃).

Priestley (1976), Potgieter and Gamble (1983), Isgor and Razaqpur (2004) and other researchers introduced the effect of average wind speed, ν (m/s) on parameter h_c, as follows:

$$h_c = 13.5 + 3.88\nu \tag{2-19}$$

Elbadry and Ghali (1983) introduced the thermal irradiation flux based on the Stefan-Boltzman radiation law, as follows:

$$q_r = C_s . e. [(T(t) + 273.15)^4 - (T_a(t) + 273.15)^4] \tag{2-20}$$

where C_s is the Stefan-Boltzman constant and e is the emissivity of gray concrete bridge surface. The emissivity of gray concrete bridge surface is equal to the ratio of the radiation of a gray body to a perfect black body at the same temperature. The modeling of the surface irradiation term of heat flow adds a nonlinearity effect due to the forth power of temperature in the equation (2-20).

The total radiation absorbed flux (the solar irradiation flux) is the complex function of various parameters (Isgor and Razaqpur 2004).

$$q_s = \alpha I_n \tag{2-21}$$

where the absorptivity parameter α is a function of the color and texture of concrete (Emerson 1973 and Priestley 1976) and I_n is the direct solar radiation intensity, which is based on the geographical location of the concrete structures (Therkeld 1970), the solar zenith angle, time of the day and many other parameters.

The nonlinearity due to the mechanical properties and natural boundaries increase the cost of thermal analysis in terms of time and complexity. Therefore, it is very important to simplify the finite element model for thermal analysis.

Hansen and Saouma (1999a) simplified modeling of the heat outflow by limiting the total flux to convection effect. Ignoring the effect of irradiation flux in thermal analysis may lead to a time lag while reaching to the maximum daily temperature.

Isgor and Razaqpur (2002) assumed that during daylight the irradiation flux approaches to zero and during the evening the solar radiation flux can be ignored. Therefore, the heat transfer analysis is not simultaneously affected by the irradiation and solar radiation flux. Also, to reduce the time of analysis, Hansen and Saouma (1999a) introduced the reference point at the critical place of each concrete sections where corrosion initiates. They used the temperature profile of the reference point as the representative of a whole section for chloride diffusion analysis.

Although the literature suggests practical techniques to simplify the heat transfer analysis, but the reliability of these suggestions has not been strongly verified. There is still an essential need to develop a comprehensive and practical model that is able to accurately calculate the temperature and heat flow at each time-step in concrete.

2.5.3 Modeling of moisture transport in concrete

Water plays an important role in the proceeding of the chemical reactions in concrete. Also, the changes of water content impact the chemical ions/substances' transport from one point to the other point in concrete. The fraction of water in concrete mixture evaporates during cement hydration. The water vapor is allocated in concrete pores and contributes to the chloride transport in concrete as well as liquid water.

The complexity of concrete medium makes it sophisticated to simulate the real physical behavior of water in concrete. There is a wide range of pore size and different phases of water including liquid and gas in concrete body. Therefore, the moisture

transport in concrete is considered as the coupled multi-phase and multi- physics problem. Several studies on moisture transport in concrete were reviewed in this research. In the simplest form, Isgor and Ghani Razaqpur (2004) assumed the moisture conductivity of concrete as a constant parameter. They considered the carbonation reaction in concrete as the source of water supply in concrete. The oversimplifying of moisture conductivity to a constant parameter results in an unrealistic simulation of complex behavior of water in concrete which is not able to capture the coupling effects of other physical parameters such as temperature on moisture transport. Xi et al. (1994) simulated the combining effects of three possible types of water conductivity in concrete, including ordinary diffusion, Knudsen diffusion, and surface diffusion on moisture conductivity, D_h , as follows:

$$D_h = \alpha_h + \beta_h \left[1.0 - 2.0^{-10.0^{\gamma_h (h-1.0)}}\right] \tag{2-22}$$

where D_h corresponds to the water conductivity when the physical field variable is relative humidity, h. Parameters α_h, β_h and γ_h are functions of the water to cement ratio. α_h is the lower bound for the diffusion coefficient. The nonlinear function of relative humidity, h shows that the potential for water transport in dry concrete almost remains constant with an increase in relative humidity. Wang and Xi (2017), proposed the empirical formula for modeling the coupling effect of temperature gradient on moisture conductivity in concrete.

The moisture transport is a complex phenomenon which is affected by a large number of parameters. In general, different scalar parameters including capillary pore pressure, P_c; relative humidity, h; total saturation degree, S_{Total}; and water content in concrete, θ_w

can be used as the physical field variable to simulate the moisture transport in concrete. A large number of studies used the water content as the most practical field variable which can easily be calibrated based on the experimentally recorded changes of water in concrete. Assuming the water transport in isotropic and non-deformable porous medium, the material dependent array, $\left[m^{(e)}\right]$ in equation (2-6) defines as the coefficient of unity array, as follows:

$$\left[m^{(e)}\right] = \alpha_p . [I] \tag{2-23}$$

where α_P is the specific water mass capacity which is equal to unity if water content in concrete, θ_w is adopted as the filed variable in moisture transport analysis.

Maekawa et al. (2009) proposed one of the most comprehensive computational models to simulate the moisture transport in porous media. They thoroughly clarified the pore size and porosity distribution in concrete segments based on a Simplistic-Rayleigh–Ritz model (Maekawa et al. 1999 and Maekawa et al. 2003). They also developed the mass and momentum conservation equations for moisture transport in concrete that consists two distinct phases of water vapor and liquid water. In order to simulate the time-dependent capillary pore pressure in concrete, Maekawa et al (2009) used the Chain rule to calculate the specific water mass capacity, α_P, as follows:

$$\alpha_P = \frac{\partial \theta_w(S_{Total})}{\partial S_{Total}} . \frac{\partial S_{Total}(h)}{\partial h} . \frac{\partial h(P_c)}{\partial P_c} \tag{2-24}$$

As shown in equation (2-25), the water content in concrete is a function of concrete porosity, liquid water density, ρ_l and total saturation degree, S_{Total}.

$$\theta_w = \text{Porosity}.\rho_l . S_{Total}(h) \quad (2\text{-}25)$$

ρ_L is the density of water in its liquid phase (Kg/m^3), which generally can be defined as a function of temperature as:

$$\rho_L = (1.545 \times 10^{-5}.T^3 - 1.85 \times 10^{-2}.T^2 + 6.65.T + 2.47 \times 10^2) \quad (2\text{-}26)$$

Using Kelvin's equation, the relative humidity is a function of capillary pressure, Pc:

$$h = h(P_c) = \exp\left(\frac{M_w P_c}{\rho_L R_g T}\right) \quad (2\text{-}27)$$

where T is temperature (K), M_w is the molecular mass of water in its liquid phase (=18.01528 gr/mol) and R_g is the universal gas constant (=8.31447).

Maekawa et al. (2009) introduced the total saturation degree as the summation of different moisture isotherms such as the condensed isotherm and the interlayer isotherm. The moisture isotherm is the definition of the saturation degree as an implicit function of relative humidity, h. The condensed isotherm corresponds to the pore water, which completely fills the capillary and gel pores with a smaller radius than the critical radius size, r_c. The concrete micro-pores are assumed as the cylindrical pores and the critical radius size, r_c, depends on the surface tension of pore microstructures (Huang et al. 2015, Maekawa et al. 2009).

In order to simulate the wide ranges of semi-cylindrical pore size in concrete, Huang et al. (2015) used the Rayleigh–Ritz model (Mindess et al. 2002) in cracked concrete, including C–S–H gel pores (smaller than 2.5 nm), small and large capillary pores and micro-cracks with widths more than 1 μm. As shown in Figure 2.4, the small capillary pores (between 2.5 and 50 nm) are the voids between C-S-H gel structures, while large capillary pores (between 50 and 140 nm) are defined as the space between cement paste particles.

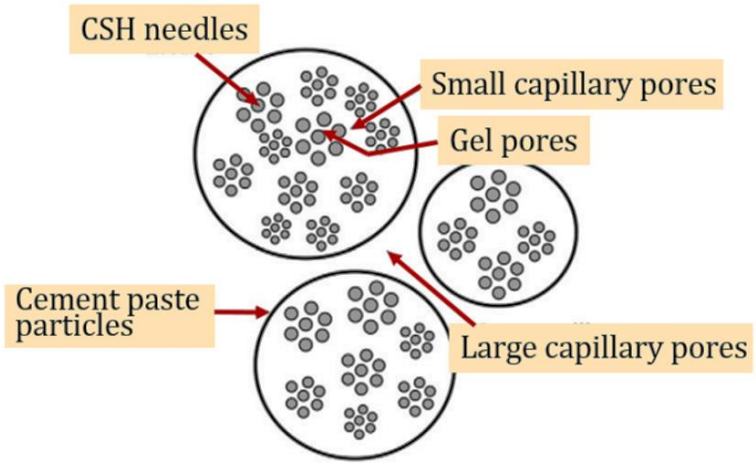

Figure 2.4: Modified Jennings' model to illustrate pore components of concrete (Garboczi and Bentz 1992)

The total saturation degree due to the condensed and absorbed water, S_c, is calculated based on the probability density function, $f_d(r)$, which consists of the total effects of different components of gel and capillary pores, as follows.

$$S_c = \frac{1}{\emptyset_t}\int_0^{r_c} f_d(r)\,.\,dr \tag{2-28}$$

$$f_d(r) = \emptyset_t \sum_{i=1}^{3} \frac{\emptyset_i}{B_i} \exp\left(-\frac{r}{B_i}\right) \tag{2-29}$$

in which $\emptyset_i$ and B_i are the porosity and peak radius at the pore distribution curve, respectively. These two parameters are calibrated based on Brunauer, Skalny and Bodor (BSB) moisture isotherm. The value of i=1, 2 and 3 refers to the gel pores, small capillary pores and large capillary pores, respectively. r_c is the critical radius size below which all these three pore components of concrete are completely saturated at specific relative humidity, h. $f_d(r)$ is a function of micro-cracks with width of larger than 1 μm to simulate the total moisture content in concrete. The schematic illustration of the probability density function, f_d with respect to the logarithm of pore radius is shown in Figure 2.5.

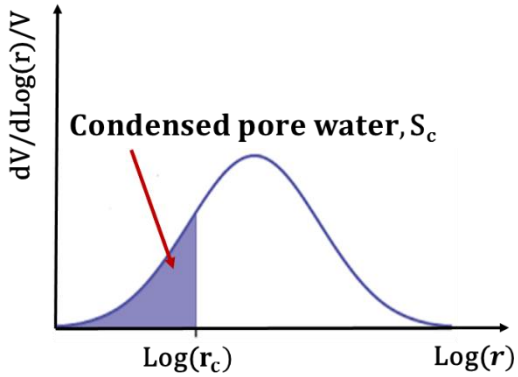

Figure 2.5: Schematic illustration of the probability density function, fd with respect to the logarithm of pore radius

The condensed water, S_c is modeled by the Brunauer, Skalny and Bodor (BSB). The BSB isotherm is the empirical equation, which has been calibrated based on the pore size and pore distribution characteristics of the concrete, and the relative humidity in the range of 5% to 100%:

$$S_c = \frac{h(1-K)[1+(C-1)k]}{(1-K.h)[1+(C-1)Kh]} \quad (2\text{-}30)$$

where h is relative humidity and K is a function of temperature, and T (°K) and C are a function of K and n_1.

$$C = \exp\left(\frac{855}{T}\right) \tag{2-31}$$

$$K = \frac{(1-1/n_1)C-1}{C-1} \tag{2-32}$$

in which n_1 is the experimentally based equation proposed by Xi et al. (1994) proposed the experimentally based equation for n_1, which illustrates the effects of curing time, cement type and water to cement ratio on condensed water, as follows:

$$n_1 = N_{tc} \times N_{ct} \times N_{wc} \tag{2-33}$$

$$N_{tc}(t_c) = 2.5 + \frac{15}{t_c} \tag{2-34}$$

$$N_{ct}(c_t) = \begin{cases} 1.1 & \text{Type I} \\ 1.0 & \text{Type II} \\ 1.15 & \text{Type III} \\ 1.5 & \text{Type IV} \end{cases} \tag{2-35}$$

$$N_{wc}\left(\frac{w}{c}\right) = 0.33 + 2.2\frac{w}{c} \tag{2-36}$$

where t_c is the curing time (days), c_t is the cement type (I, II, III or IV) and w/c is the water to cement ratio.

The hysteresis behavior of moisture isotherms is referred as the difference between the isothermal path under wetting and drying conditions. This difference is mainly due to

the entrapment of water in the gel pore structures. The hysteresis behavior of water in concrete depends on the different scenario as mentioned below:

Scenario 1: the virgin wetting path (primary wetting loop).

Scenario 2: the virgin drying path (primary drying loop).

Scenario 3: the scanning curves with a completely dry stage as their starting point.

Scenario 4: the scanning curves with a completely wet stage as their starting point.

Typically, during wetting scenario, the BSB isotherm is able to accurately simulate total saturation degree in wetting scenario. However, in drying conditions, the total saturation degree is impacted by not only the condensed water, but also the trapped water in concrete pore channels, due to the so-called ink-bottle effect. During drying condition, the larger pores remain fully saturated until the water in the smaller pores gradually evaporates. As shown in Figure 2.6, during the drying stage, the water blocked in the larger concrete pores which are connected to the smaller pores (with radius less than r_c). Since the BSB moisture isotherm is calibrated to calculate the condensed water in concrete pores with radius smaller than r_c, it is not able to capture the significant amount of trapped water in large pores.

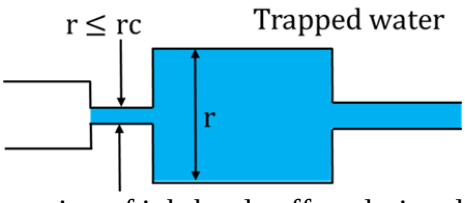

Figure 2.6: Schematic illustration of ink-bottle effect during drying stage

As shown in Figure 2.7, compare to the wetting stage, during the drying condition, the water content and so the saturation degree of concrete body is higher due the water which is trapped in larger pores. Therefore, the BSB moisture isotherm is not able to capture the real amount of water content in concrete. Consequently, defining another isotherm to simulate the effect of trapped water on total the water content is required.

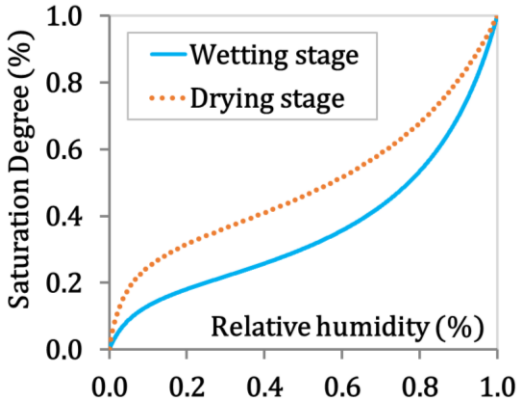

Figure 2.7: Schematic illustration of the effect of hysteresis behavior of moisture isotherms during drying stage on moisture transport analysis

Maekawa et al. (2009) proposed the empirical formulation to simulate the hysteresis behavior of the ink-bottle isotherm, S_{ink} is as shown in the equations (2-37):

$$S_{ink} = \begin{cases} 0 & \text{Scenario 1} \\ -S_c \mathrm{Ln}(S_c) & \text{Scenario 2} \\ S_c(\mathrm{Ln}(S_{r_{max}}) - \mathrm{Ln}(S_c)) & \text{Scenario 3} \\ -S_{r_{min}} \mathrm{Ln}(S_c) & \text{Scenario 4} \end{cases} \quad (2\text{-}37)$$

where, $S_{r_{max}}$ is the maximum saturation degree of concrete during the wetting stage. r_{max} corresponds to the pore size, which the pores with larger radius r_{max} never have been completely saturated. $S_{r_{min}}$ is the minimum saturation degree of concrete during the

wetting-drying scenario r_{min} corresponds to smallest pore size, which have experienced the minimum water content during drying cycles.

The total condensed water is equal to the summation of contribution of both BSB isotherm and ink-bottle isotherm, as follows:

$$S_c = S_c + S_{ink} \tag{2-38}$$

Furthermore, the interlayer isotherm is the enhanced moisture isotherm that simulates the hysteresis behavior of water in the C-S-H structures of gel pores. The huge surface area of gel pores significantly influences the water removal and re-entry into the layers of pore structure during drying or wetting stages (Maekawa et al. 2009). Based on the equation (2-39), the interlayer isotherm, S_{Lr} depends on S_{min} and h_{min} which are the minimum interlayer saturation degree and the minimum relative humidity, respectively, and S_{max} is the maximum amount of interlayer water volume fraction during the drying-wetting loops.

$$S_{Lr} = \begin{cases} h & \text{Scenario 1} \\ h^{0.05} & \text{Scenario 2} \\ 1 + (h-1)\frac{(S_{min}-1)}{(h_{min}-1)} & \text{Scenario 3} \\ S_{max}.h^{0.05} & \text{Scenario 4} \end{cases} \tag{2-39}$$

determining the condensed isotherm and the hysteresis isotherms, Maekawa et al. (2009) calculated the total saturation degree, S_{Total}, as follows:

$$S_{Total} = \frac{(\emptyset_{Paste} S_c + \emptyset_{Lr} S_{Lr})}{Porosity} \tag{2-40}$$

where $\emptyset_{Lr}$ is the interlayer porosity and $\emptyset_{Paste}$ is the paste porosity, which is the summation of gel porosities, $\emptyset_{gell}$; small capillary pores porosities, $\emptyset_{small,cp}$; and large capillary pores porosities, $\emptyset_{large,cp}$. The total concrete porosity is a summation of these two terms:

$$\emptyset_{Paste} = \emptyset_{gell} + \emptyset_{small,cp} + \emptyset_{large,cp} \quad (2\text{-}41)$$

$$\text{Porosity} = \emptyset_{Paste} + \emptyset_{Lr} \quad (2\text{-}42)$$

Maekawa et al. (2009) also introduced the empirical formulations to simulate the moisture diffusion coefficient, D_p as a summation of water liquid conductivity, K_L and water vapor conductivity, K_V, as follows:

$$D_P = K_L(P_c) + K_V(P_c) \quad (2\text{-}43)$$

Furthermore, Maekawa et al (2009) proposed the equation to simulate the exposure conditions at the concrete surfaces. They introduced the convection flux, q_s, as a linear function of the difference between the ambient relative humidity, h_s, and the relative humidity at concrete surface, h. E_b is the emissivity coefficient which is experimentally calibrated by Maekawa et al. (2009) to the constant value = 5.E-5.

$$q_s = -E_b(h - h_s) \quad (2\text{-}44)$$

There are some comments and criticisms regarding the proposed algorithm by Maekawa et al. (2009). The α_P and D_P parameters in their algorithm comprised many

variables, most of which are rarely used in practical engineering problems. Furthermore, due to the lack of supplementary documents, the accuracy and flexibility of the computational algorithm to simulate the real physical behavior of moisture transport in concrete is a matter of concern.

In another effort, Michel et al. (2013) proposed a numerical model based on their experimental verifications to simulate the behavior of moisture in cracked concrete. They also recommended a new moisture isotherm based on a bimodal function of a van Genuchten type (Van Genuchten 1980). They modeled the moisture transport in cracked concrete. The free surface boundaries where moisture penetrates to the concrete is called "a coalesced crack length". They concluded that the increase in the crack width and crack propagation result in elevated water content in concrete environment. In the computational model proposed by Michel et al. (2013), the total water content in concrete is estimated as a nonlinear function of capillary pressure including three constant parameters, which are calibrated based on the experimental tests. Also, they introduced the integral-based equations to determine the moisture conductivity coefficient as the summation of the liquid water and vapor conductivity terms.

In the computational model developed by Huang et al. (2015) the pore distribution and physical behavior of the cracked concrete is well-defined. However, the moisture diffusion coefficient is not considered in their study. As the moisture diffusion coefficient is calculated due to an integral-based equation, it is challenging to apply this term for

liquid water and vapor conductivity. Also, their model is not able to capture the drying-wetting hysteresis effects on the total moisture content in concrete.

On the other hand, Hall and D. Hoff (2012) removed the difficulties of the calculation of liquid water and vapor conductivity terms by proposing the practical equations. Also, in their proposed formulations, the moisture diffusion coefficient is estimated regardless of pore size distribution characteristics.

2.5.4 Modeling of chloride transport in concrete

Free chloride ions transport through concrete pore channels as the result of electro-magnetic force, diffusion and advection. The effect of gravity on chloride transport through concrete pore channels is negligible. As shown in Figure 2.8, the concrete pore wall structure has positive electric charge, while the chloride ions have negative electric charge. When concrete surfaces are exposed to chloride attack, due to the electro-magnetic force between the positive and negative electric charges, chloride ions are attracted toward the concrete pore channels (Maekawa et al., 2009).

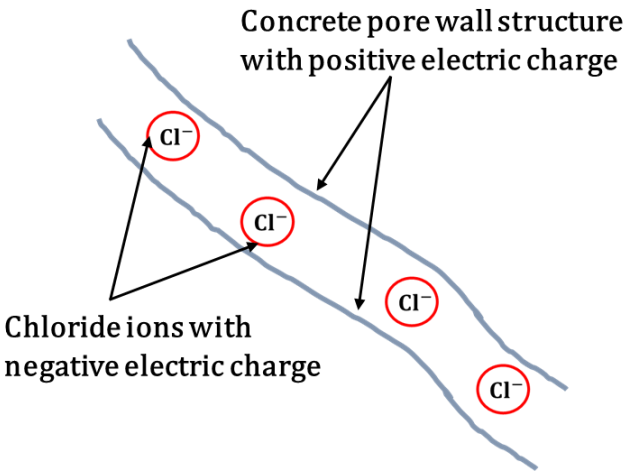

Figure 2.8: Schematic illustration of chloride transport through concrete pore channels due to the effect of electro-magnetic force

The schematic illustration of diffusive and advective transport of chloride ions in concrete are shown in Figure 2.9 (a) and (b), respectively. Due to the concentration gradient, dissolved chloride ions/chemical substances in stationary water inside concrete pores can diffuse from the elevated concentration points to the points with lower concentration, while in the advective transport, chloride ions move with water velocity in concrete.

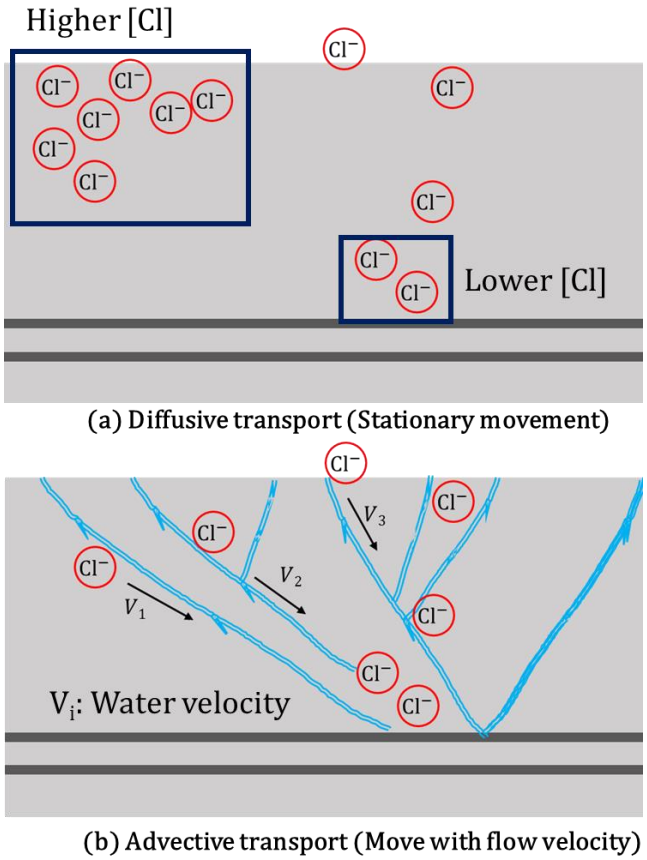

Figure 2.9: Schematic illustration of (a) diffusive transport and (b) advective transport of chloride ions in concrete

Generally, chloride ion transport in concrete is a multi- physics phenomenon. Chloride transport is also affected by cracking in concrete, so the chloride transport is generally impacted by the stress distribution and crack propagation of concrete. Also, the environmental exposure conditions around concrete surfaces such as the ambient temperature and relative humidity influence the chloride transport in concrete.

When concrete is exposed to de-icing salts or sea-water, chloride ions can penetrate to steel bars through diffusion and advection. The diffusion of chloride ions in concrete is computed by the general Helmholtz equation, which is simplified based on the Fick's law

(Hansen and Saouma, 1999a). Monitoring chloride concentration along the steel bars is significant in estimation of time of corrosion initiation, as free chloride ions dissolve in water and flow through concrete pores channels.

When the chloride content at the surface of steel bars exceeds the threshold value, the protective layer of steel bars depassivates. According to Maekawa et al. (2009), the chloride content is combination of the free chloride ions and the binding chloride. Free chloride ions can freely move in concrete, while binding chloride is chemically attached to the concrete pore wall structures and can only contribute to the initial stage of corrosion, when the pH of the concrete medium is 13. During the coupled chloride-induced and carbonation-induced corrosion, the production of carbonic acid, H_2CO_3, significantly lowers the pH in concrete (from 13 to 8). As a consequence, the chemical bounds of binding chlorides break down and then binding chloride contributes to the corrosion process (Collepardi et al. 1972).

The simplest approach to model the chloride diffusion coefficient is to consider it as a constant parameter. Also, it can be modeled as a time-dependent function of w/c or additive materials, like fly ash or slag (Hansen and Saouma 1999a, Mangat and Molloy 1994, Luping and Gulikers 2007). To improve the modeling of chloride diffusion, the coupling effect of thermal analysis on the time-dependent chloride diffusion coefficient is considered by Hansen and Saouma (1999a), Tang and Nilsson (1994) and Saetta et al. (1993). Others studied the effect of aggregate on chloride diffusion in concrete (Samson and Marchand 2003, Care 2003 and Jang et al. 2011). In porous concrete medium, the

aggregate proportioning and distribution affect the crack geometry and interaction of aggregate and cement paste. As illustrated in Figure 2.10, Li (2002) simplified the concrete cracks to the straight channels.

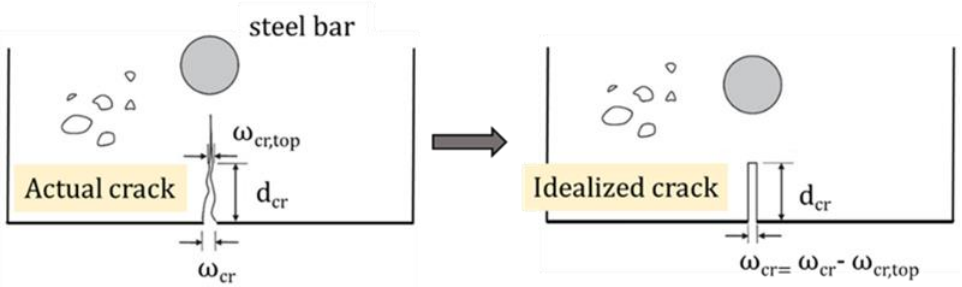

Figure 2.10: Simplification of idealized crack to straight channel (Jang et al. 2011)

If the size of a crack exceeds the threshold value, which is around 55–80 μm (Jang et al. 2011) or mm scale (Maekawa et al. 2009), the effect of crack on the chloride diffusion coefficient is significant. Kwon et al. (2009) simulated the effect of concrete crack width on the chloride diffusion coefficient, as follows:

$$D_{Cl} = D_{Cl}.\ f_{crack}(w_{cr}) \tag{2-45}$$

where f_{crack} is the nonlinear function of crack width, w_{crack} (mm):

$$f_{crack} = 31.61{w_{crack}}^2 + 4.73w_{crack} + 1.0 \tag{2-46}$$

Also, Li (2002) introduced the "crack geometry factor" to evaluate crack diffusion characteristics like the connectivity of different channels, tortuosity and constrictivity. As shown in Figure 2.11, porosity is the fraction of pore volume to total concrete volume. Tortuosity is referred as the difficulties in ion diffusion due to the increase in length and

complexity of diffusion path, while constrictivity corresponds to the interaction of pore structures with chemical ions. Maekawa et al. (2009) proposed empirical equations for concrete porosity, tortuosity and constrictivity to computationally simulate the coupling effects of pore structures and pore geometric properties on chemical ion diffusion in concrete.

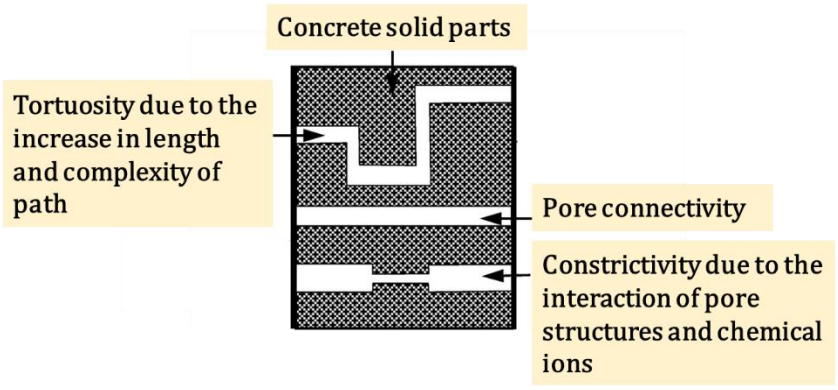

Figure 2.11: Schematic illustration of the influential parameters of the pore network on chloride diffusion (McCarter and Garvin 1989)

In a more comprehensive manner, the effects of many other factors on chloride diffusion analysis were investigated. Broomfield (2007) generated the Life-365 software to model the effects of additive material, age of concrete and exposure conditions on predicting the time on the initiation stage chloride-induced corrosion. Na et al. (2017) developed the finite element model to simulate the realistic behavior of an existing bridge under chloride attack. He applied the equation proposed by Xi and Bazant (1999), in which the diffusion coefficient is a function of curing time (t_0), volume fraction of aggregate (g_i), relative humidity (HR), temperature (T) and free chloride in concrete (C_f), as shown in equation (2-47).

$$D_{Cl} = f_1(^{w}/_{c}, t_0).f_2(g_i).f_3(HR).f_4(T).f_5(C_f) \quad (2\text{-}47)$$

Mingzhong and Guang (2010) introduced the HYMOSTRUC3D model to predict time-transient analysis of chloride diffusion in a three dimensional environment of saturated cement paste. The influence of age and water to cement ratio of concrete and the effect of chloride ion conductivity on the chloride diffusion coefficient was verified and the results were in good agreement with their experimental data. Christensen (1979) and Zheng et al. (2010) proposed the advanced equations to calculate the reduction factor due to the interaction between calcium-silicate-hydrate gels (C-S-H) and chloride ions. Moreover, Garboczi and Bentz (1992) simplified the interaction of C-S-H and chloride ions by suggesting the reduction factor of 1/400 which should be multiplied by the chloride diffusion coefficient.

Michel et al. (2013) introduced an equation considering the binding chloride effect on diffusion characteristics of concrete. Although the effect of binding chloride is not significant on the initiation of corrosion, in the presence of a significant amount of carbonic acid or other types of acid, the dissolved binding chloride actively collaborates in chloride diffusion and so the total chloride content which contribute to the chloride-induced corrosion increases (Luo et al. 2003).

Michel et al. (2013) calibrated the parameters of the equation proposed by Glass and Buenfeld (2000) for only some specific types of cement. Maekawa et al. (2009) proposed the nonlinear model of binding chloride for various types of cement admixtures and proportions. Moreover, Maekawa et al. (2009) proposed the enhanced model for chloride

diffusion and advection analysis through a porous concrete medium by considering the coupling effects of temperature, crack width, pore distribution, tortuosity, constrictivity and saturation degree.

Based on the experimental tests by Maruya et al. (1998), Maekawa et al. (2009) introduced the chloride flux at concrete surfaces, q_{Cl} as the summation of the diffusive component, q_{diff}, and the quasi-adsorption flux, q_{ads}, as follows:

$$q_{Cl} = q_{diff} + q_{ads} \tag{2-48}$$

$$q_{diff} = -E_{Cl}.(C_{Cl} - C_s) \tag{2-49}$$

$$q_{ads} = K_{Cl}.(\frac{C_{Cl}}{C_0})^2 \exp(-1.15C_{Cl}) \tag{2-50}$$

where C_{Cl} is the chloride concentration, C_s is the ambient chloride concentration, E_{Cl} is the emmisivity coefficient of chloride flux $E_{Cl.}$ Maekawa et al. (2009) suggested the emissivity coefficient, E_{Cl} equal to 1.0E-6. They proposed empirical equations to estimate the parameter K_{Cl} as a function of cement admixture. Accumulation of chloride ions at concrete surface results in the neutralization of the positive electric charge of concrete pore wall structures. Therefore, the electric-magnetic force reduces and so, the adsorption of chloride ions at concrete surfaces decreases. The quasi-adsorption flux models the effect of chloride accumulation at concrete surface on reduction of chloride diffusion in concrete. However, the proposed equation by Maekawa et al. (2009) for the quasi-adsorption flux, q_{ads} is not able to precisely simulate the reduction in chloride adsorption

by increase in chloride accumulation at concrete surfaces. As shown in Figure 2.12, the proposed equation of quasi-adsorption is not the decreasing function of chloride concentration.

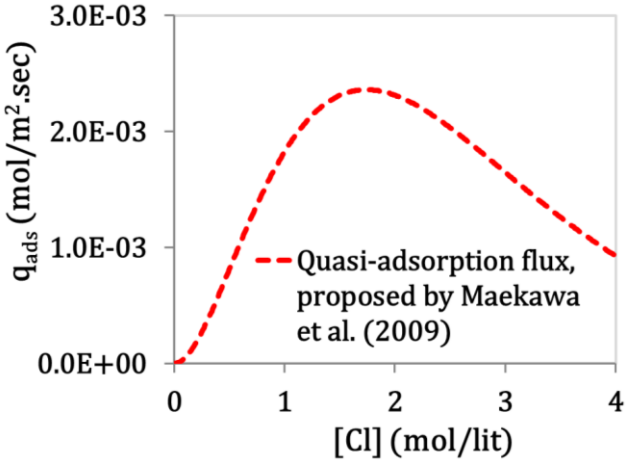

Figure 2.12: Schematic illustration of the quasi-adsorption flux as the nonlinear function of chloride concentration, [Cl], proposed by Maekawa et al. (2009)

2.5.5 Modeling of oxygen diffusion in concrete

Oxygen is a critical chemical substance in corrosion procedure, as it is required for both the corrosion initiation and process of corrosion. The rate of steel corrosion in concrete significantly decreases by diminution of oxygen in concrete, even in the presence of sufficient water. As the water content increases, there is less space for dissolved oxygen to penetrate and diffuse in concrete medium. Therefore, the time-transient changes of the oxygen concentration along the steel bars in concrete structures is prominent in health monitoring of concrete structures (Ji 2006).

In general, the Fick's law governs the diffusion of oxygen and other chemical substances in concrete. The accurate modeling of the oxygen diffusion coefficient, based

on the characteristics of concrete body and boundary conditions are the main challenges to simulate the oxygen diffusion in concrete. Papadakis et al. (1991) simulated the oxygen diffusion coefficient as a function of time-dependent concrete porosity and relative humidity. They introduced the concrete porosity as a function of the water-to-cement ratio (w/c), aggregate-to-cement ratio, cement and aggregate densities and entrapped air in concrete. Cement hydration and carbonation alter the porosity during the time of analysis. Isgor and Ghani Razaqpur (2004) introduced the decay factor to define the effect of carbonation-induced corrosion on porosity changes. Pour-Ghaz (2007) defined the oxygen diffusion coefficient based on the temperature and water to cement ratio. Generally, the sufficiency of oxygen to reduce the reaction rate in electrochemical cells during service life of concrete only matters in submerged structures.

2.6 Chemistry of chloride-induced corrosion in concrete

If chloride concentration along steel bars is above the threshold value, in presence of sufficient oxygen and water, the electrochemical cell is formed in the vicinity of steel bars. As is shown in Figure 2. 13, the electrochemical cell consists of steel bars (iron), dissolved oxygen (O_2) and moisture in concrete (H_2O).

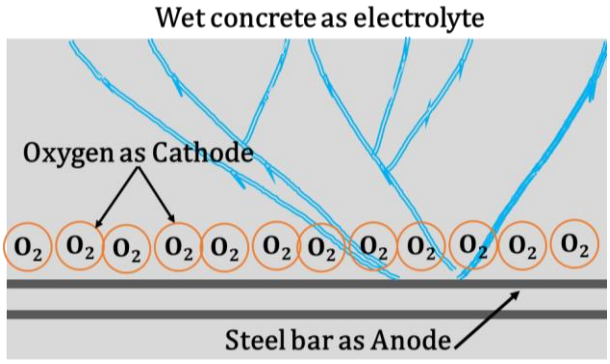

Figure 2.13: Schematic illustration of electrochemical cells along steel bars in concrete

Generally, the electrochemical cell includes an ionic conductor, called an electrolyte, and two distinct electrodes with different voltage potentials, which are called "Anode" and "Cathode" (Isgor and Razaqpur 2005). The iron in the steel bars is the anodic electrode, while the dissolved oxygen around the surfaces of steel bars is the cathodic electrode. The electrolyte is the wet concrete adjacent to steel bars. The electrochemical mechanism of chloride-induced corrosion in concrete is shown in Figure 2.14, and the anodic and cathodic reactions in each electrode are mentioned as follows:

$$Fe(s) \rightarrow Fe^{2+}(aq) + e \qquad \text{Oxidation; anodic reaction} \qquad (2\text{-}51)$$

$$O_2(g) + 2H_2O(l) + 4e = 4OH^-(aq) \qquad \text{Reduction; cathodic reaction} \qquad (2\text{-}52)$$

$$Fe^{2+}(aq) + 2OH^-(aq) \rightarrow Fe(OH)_2 \qquad (2\text{-}53)$$

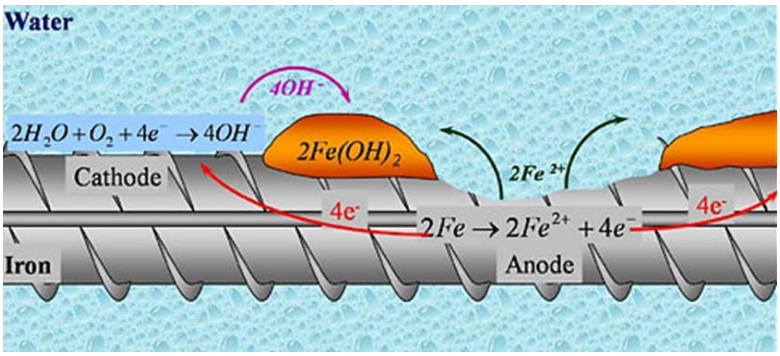

Figure 2.14: Schematic illustration of the electrochemical mechanism of chloride-induced corrosion in concrete (PCA 2017)

As is shown in Figure 2.12, the electrons which are released from the anodic site, are absorbed by the cathodic electrode, while the hydroxyl ions flow from cathode to anode. The anodic and cathodic sites are located at the surface of steel bars. Anode forms at the weak points with the higher risk of corrosion. The weak points corresponds to the concrete locations with the higher risk of corrosion due to any of small pH value, higher chloride content or other salt concentrations, the cracked or opening area with residual stress. On the other hand, cathode forms around steel bars where oxygen accumulates.

When corrosion initiates, the electrons which are released from anode in the oxidation reaction are consumed in reduction process in cathodic sites. To reach the electric balance in an electrochemical cell, the hydroxyl ions with negative electric charge move to the anodic sites through the water in adjacent concrete pores. $Fe(OH)_2$ is the initial product of the corrosion and has a high tendency to react with water and oxygen. As shown in equations (2-54) and (2-55), Ferrous ions react within the pore solution below to produce Fe_2O_3 or the red rust.

$$4Fe(OH)_2 + 2H_2O + O_2 \rightarrow 4Fe(OH)_3 \quad (2\text{-}54)$$

$$2Fe(OH)_3 \rightarrow 2H_2O + Fe_2O_3.H_2O \quad (2\text{-}55)$$

Red rust is the final product of chloride-induced corrosion in concrete and has the volume of approximately four times greater than sound steel bars with the same mass. The volume expansion due to steel corrosion increases the internal stresses and consequently, the risk of cracking and spalling of concrete adjacent to steel bars (Hansen and Saouma 1999, Bazant 1979).

In addition to the reduction and oxidation reactions, chloride ions tend to chemically combine with iron ions in electrochemical cells (Bentur et al., 1997), as follows:

$$Fe^{2+} + 2Cl^- \rightarrow FeCl_2 \quad (2\text{-}56)$$

In order to compensate the lack of iron ions which are consumed in the chemical reaction, the reduction reaction at anodic sites should proceed in forward direction. Consequentially, chloride ions contribute to the corrosion process by motivating the electrochemical reaction at anodic reaction.

2.7 Polarization and over-potential

The standard cell potential (Maekawa et al. 2009) or the open-circuit potential (Pour-Ghaz 2007) refers to the potential of the electrodes when there is no electron movement in electrochemical cell. The anodic and cathodic potentials are initialized to the standard

cell potential of iron and oxygen based on a reference electrode (Pour-Ghaz 2007, Maekawae et al. 2009, Hansen and Saouma 1999b).

Initially, the anodic standard cell potential is negative, whereas it is positive for the cathodic one. In an electrochemical cell, the net current occurs due to electron transfer, with negative charge, from anode to cathode. By its very nature, without altering velocity, the iron ions with positive electric charge tend to move from the cathodic sites with higher electric potential region to the anodic site, where there is lower electric potential. The electron ions, as the negative electric charge particles follow the reverse path from anode to cathode. This electrical current tends to alter the potential at both of the electrodes; therefore, the potential at anode turns more positive, while the potential at the cathode turns more negative.

The changes of potential from its initial value are called “Polarization” (Dao et al. 2010). Three major types of electrode polarization are introduced to model steel corrosion in concrete structures; activation polarization, concentration or "diffusion overpotential" or "mass-transport overpotential” (Ji 2006); and resistance or “IR drop” or “Ohmic potential drop” polarization (Uhlig and Revie 1985).

According to the Nernst’s law, the activation polarization is the potential change due to the activation energy of each electrode (Maekawa et al. 2009). By definition, both the anodic and cathodic polarizations are shifted by the activation polarization. Concentration polarization is caused by insufficient reactants at the electrodes for processing the chemical reactions in forward direction. In order to compensate the insufficiency of

chemical reactants, the electrochemical reactions at the electrode proceeds in the reverse direction. The resistance polarization quantitatively measures the tendency of the electrodes to remain their initial conditions. The net electrical flow between the electrodes approaches zero if the electrolyte in electrochemical cell has enormous resistance. The effect of resistance polarization can be ignored when the anodic and cathodic sites are adjacent to each other (Ji 2006).

In the electrochemical mechanism of steel corrosion in concrete, the initial electric potential at the anode and cathode electrodes are altered by releasing or absorbing the electric charge particles. Therefore, it is necessary to consider the activation polarization effect on the potential change of both sides of the electrochemical cell (Silva 2013, Tuutti 1982, Li 2002, Broomfield 2007, Uhlig and Revie 1985, Isgor and Ghani Razaqpur 2002, Saetta and Vitaliani 2004 and etc.).

The concentration polarization in concrete can be defined as a function of oxygen concentration in concrete during the corrosion process. Due to the consumption of oxygen at cathodic sites, the amount of oxygen may be insufficient to proceed the cathodic reaction. In this case, the oxidation reaction turns in the reverse direction to compensate oxygen deficiency (Dao et al. 2010- b, Pour-Ghaz 2007).

2.8 Tafel diagram for determination of corrosion current

The changes of electrode potentials in an electrochemical cell due to the different polarization effects can be introduced as functions of current density, which is equal to

the current network between the electrodes per unit area of each electrode (Maekawa et al. 2009). Tafel diagram is a practical and useful technique to depict the changes of anodic and cathodic electric potentials correspond to current density. Figure 2.15 shows the specific characteristics of different polarization terms on the Tafel diagram.

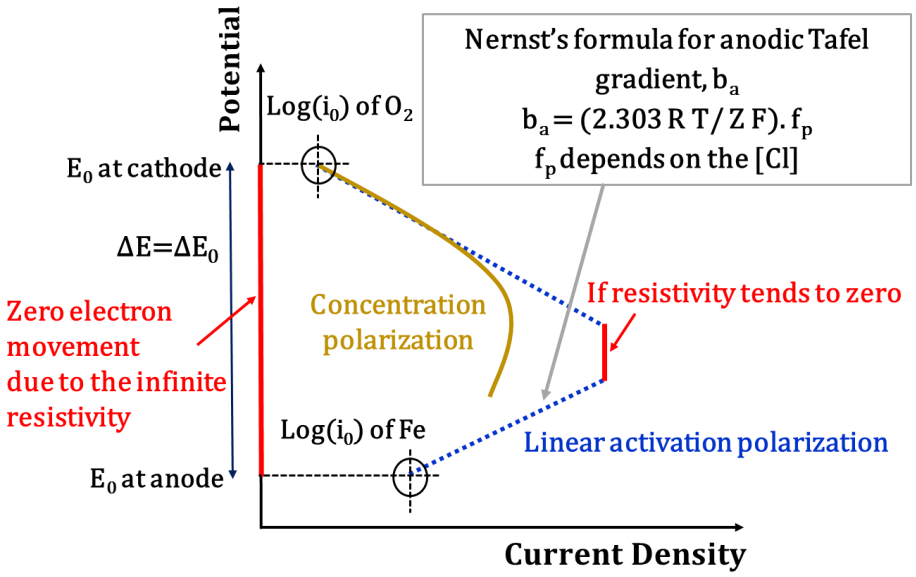

Figure 2.15: Schematic illustration of the Tafel diagram and three terms of polarization including activation polarization, concentration polarization and resistance polarization

As the result of electron movement inside the electrochemical cell in concrete, the electric potential at anodic and cathodic electrodes are changed from the initial values, E^0_{Fe} and $E^0_{O_2}$, which are the standard cell potentials of anodic and cathodic electrodes in 25℃, respectively.

In case of very large electrolyte resistivity, electrons cannot easily move inside the electrolyte. Therefore, the electrode potentials remain constant in open-circuit potential conditions. In the case of extremely close distance between the anodic and cathodic sites

or very low concrete electrical conductivity, the effect of resistance polarization is ignored in changes of electrodes potentials (Pour-Ghaz 2007). As Figure 2.13 shows, the gap between two activation polarization lines in the Tafel diagram illustrates the resistance polarization. The nonzero resistance polarization prevents the anodic and cathodic straight lines to approach and coincide each other.

The effect of concentration polarization is schematically shown in Figure 2.13 as well. In the presence of sufficient oxygen, the potential changes are governed by the activation polarization effect, and the corrosion is called activation-controlled process. In the activation-controlled process, if electrons dominate the electrolyte resistance, the potential changes of the anodic and cathodic electrodes due to the activation polarization with the current density is defined by straight lines in the Tafel diagram (Millard et al. 2001). Following the Nernst's equation, the anodic and cathodic potentials are changed as the linear functions of the activation energy and temperature. As shown in Figure 2.16, the slopes of these two straight lines are named as "β_a" and "β_c", which are the anodic Tafel slope and the cathodic Tafel slope, respectively. Maekawa et al. (2009) simulated the effect of chloride content in concrete on the anodic Tafel slope, β_a. They introduced the numerical equation to model the dependency of the anodic Tafel slope on the time-dependent chloride concentration along steel bars in concrete.

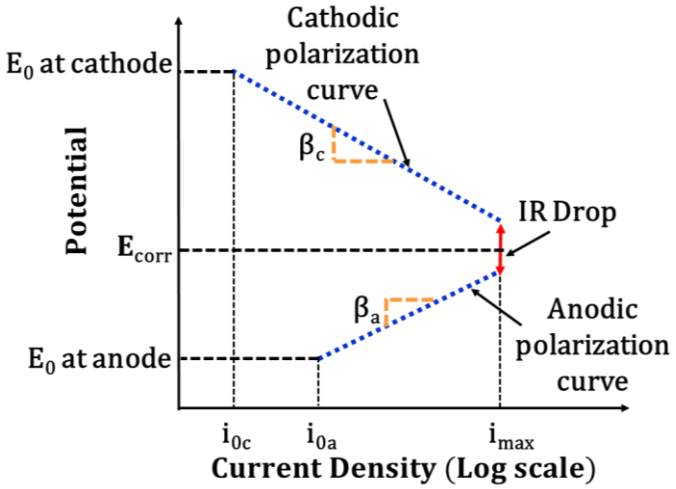

Figure 2.16: Schematic illustration of the activation polarization straight lines and the resistance polarization effect in the Tafel diagram (reproduced from Pour-Ghaz 2007)

However, due to the lack of oxygen at cathode, the concentration polarization term dominates the activation polarization and changes the linear pattern of the cathodic polarization. At the cathodic site, the straight line which initiates from the standard cell potential, suddenly falls down to the specific current density amount, called "Limiting current density" as shown in Figure 2.17. In concentration-controlled or cathodic controlled (Broomfield 2007) corrosion, the effect of concentration polarization directly rises by increase in consumption of oxygen at cathodic sites during service life of concrete structures. Increasing the concentration polarization causes the reduction of the limiting current density (Pour-Ghaz 2007, Isgor and Ghani Razaqpur 2006, Ji 2006).

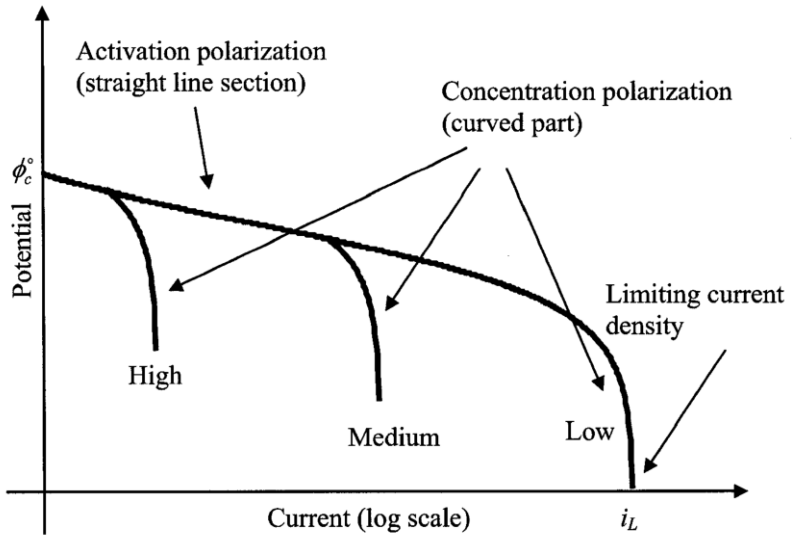

Figure 2.17: Schematic illustration of the concentration polarization effect (Pour-Ghaz 2007)

The final goal of modeling steel corrosion in concrete structures is estimating the reduction of reinforcing steel cross sections during the service-life of concrete structures. The polarization effects, which depend on the time-transient environmental and exposure conditions, govern the corrosion process and rate of corrosion. For this purpose, Isgor and Ghani Razaqpur (2006) introduced five coupling steps for time-transient modeling of chloride-induced corrosion in concrete:

1. modeling the initiation stage of corrosion and the influential environmental parameters
2. modeling the polarization effects and evaluating if any specific polarization term controls the corrosion process
3. calculating the electric potential distribution along steel bars
4. calculating the anodic and cathodic current densities based on Ohm's Law

5. calculating the corrosion rate and rate of iron reduction

The potential characteristics of the anodic and cathodic electrodes depend on the polarization effects. The potential distribution, $\emptyset(x, y, z)$, along the steel bars and corroded regions can be obtained at each time step of analysis by solving Laplace's equation based on the electrical charge conservation law (Doa et al. 2010b), following as below:

$$\nabla^2 \emptyset = 0.0 \tag{2-57}$$

Ignoring the effect of resistance polarization, Doa et al. (2010b) defined the boundary conditions at the anodes and cathodes, as follows:

$$E_{Fe} = E_{Fe}^0 + \beta_a \log\left(\frac{i_a}{i_0^a}\right) \tag{2-58}$$

$$E_{O_2} = E_{O_2}^0 + \beta_c \log\left(\frac{i_c}{i_0^c}\right) - \frac{2.303RT}{Z_{O_2}F} \log\frac{i_L}{i_L - i_c} \tag{2-59}$$

where E_{Fe}^0 is the anodic standard cell potential (volts) and $E_{O_2}^0$ is the cathodic standard cell potential (volts). i_a and i_c are the time-dependent current densities at the anodes and cathodes (A/m^2), respectively. i_0^a and i_0^c, are referred as the equilibrium exchange current densities at anode and cathode, when the corresponding electrode potentials are equal to the open-circuit potentials. β_a and β_c are the anodic and the cathodic Tafel gradient, respectively. In equation (2-59), the term $-\frac{2.303RT}{Z_{O_2}F} \log\frac{i_L}{i_L - i_c}$ demonstrates the nonlinearity due to the concentration polarization effect where i_L is the limiting current density (A/m^2),

R is the universal gas constant (=8.314 J/(mol.K)), Z_{O_2} is the number of electrical charge of oxygen (= 2), F is Faraday's constant (=9.65E+4 C/mol) and T is temperature (°K).

Table 2.2 summarize the kinetics of corrosion assuming that the effect of resistance polarization is not considerable. Where $\emptyset^{aa}$ and $\emptyset^{ca}$ are the anodic and cathodic activation polarization terms, respectively, while $\emptyset^{cc}$ represents the concentration polarization at cathodic sites.

Table 2.2: Different polarization terms in anodic and cathodic electrodes in electrochemical mechanism in concrete(Stern and Geary 1957, Doa et al. 2010b)

Reaction		Anodic site	Cathodic site
		$Fe(s) \rightarrow Fe^{2+}(aq) + e(pt)$	$O_2(g) + 2H_2O(l) + 4e(pt) = 4OH^-(aq)$
Polarization	Activation	$\emptyset^{aa} = \beta_a \log(\frac{i_a}{i_0^a})$	$\emptyset^{ca} = \beta_c \log(\frac{i_c}{i_0^c})$
	Concentration		$\emptyset^{cc} = -\frac{2.303RT}{Z_{O_2}F} \log \frac{i_L}{i_L - i_c}$
Stern and Geary relation for potential-current density relation		$E_{Fe} = E_{Fe}^0 + \emptyset^{aa}$	$E_{O_2} = E_{O_2}^0 + \emptyset^{ca} + \emptyset^{cc}$

Munn and Devereux (1991) suggested applying the Ohm's law for calculation of the current density at each node along the steel bars, i (A/m^2), as follows:

$$i = -\frac{1.0}{\rho}\frac{\partial \emptyset}{\partial n} \quad (2\text{-}60)$$

where ρ is the concrete resistivity and n is the direction vector normal to the steel bar sections. The corrosion current density and the corrosion rate can be determined as functions of the anodic current density.

Many studies including Michel et al. (2013), Hansen and Saoumo (1999- b), Pour-Ghaz et al. (2009), Isgor and Ghani Razaqpur (2006), Doa et al. (2010) computationally modeled the complicated internal boundary conditions at the anodic and cathodic sites. Also, they have simulated the coupling effects of concrete properties (i.e., resistivity, aggregate volume and fraction) and environmental conditions, such as temperature, humidity, chloride content by complex nonlinear finite element analysis. However, the practicality of their models is still a matter of concern.

Maekawa et al. (2009) assumed that in the presence of sufficient amount of oxygen, the cathodic boundary conditions is simplified by ignoring the concentration polarization effect. Also, the anodic and cathodic sites are assumed in close distant, so the resistance polarization term approaches zero. These assumptions make it possible to simplify the modeling of steel chloride-induced corrosion for practical engineering problems such as the chloride-induced corrosion in concrete bridge decks. Maekawa et al. (2009) proposed the two straight lines to illustrate the anodic and cathodic activation polarization terms by ignoring the concentration polarization and resistance polarization terms. As shown in Figure 2.18, these two lines intersect each other at the specific point which corresponds to the main characteristics of corrosion including corrosion potential, $E_{corr}(t)$ and corrosion current density, $i_{corr}(t)$, where these two parameters are the implicit functions of time, t.

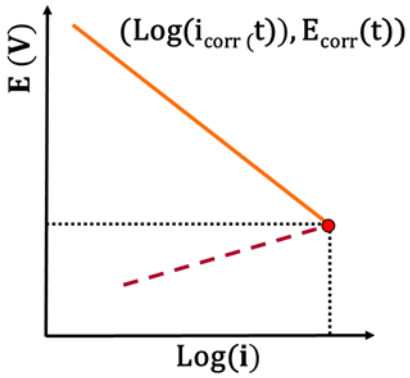

Figure 2.18: Schematic illustration of the main characteristics of corrosion including corrosion potential, Ecorr(t) and corrosion current density, icorr(t), in the Tafel diagram (Maekawa et. al 2009)

In the corrosion algorithm proposed by Maekawa et al. (2009), the Nernst's method expresses the electrode potential as a function of electric current density, as follows:

$$\emptyset^{a} = \left(\frac{2.303RT}{0.5Z_{Fe}F}\right)\log\left(\frac{i_a}{i_0^a}\right) \tag{2-61}$$

$$\emptyset^{c} = -\left(\frac{2.303RT}{0.5Z_{O_2}F}\right)\log\left(\frac{i_c}{i_0^c}\right) \tag{2-62}$$

where $\emptyset^{a}$ and $\emptyset^{c}$ are the anodic and cathodic polarization, respectively. i_a and i_c are the corresponding anodic and cathodic electric current densities (A/m^2). i_0^a and i_0^c are equilibrium exchange electric current densities at anode and cathode ($i_0^a = 1.0 \times 10^{-5}\ {}^{A}/_{m^2}$ and $i_0^c = 1.0 \times 10^{-10}\ {}^{A}/_{m^2}$ at 20˚C). Z_{Fe} is the number of electric charge of iron ion (=2) and Z_{O_2} is the number of electric charge of oxygen (=2). The corrosion potential, $E_{corr,}$ and corrosion current density, $i_{corr,}$ are calculated as the result of linear equation that defines the coordinates of the intersection points in the Tafel diagram.

$$E_{corr} - E_{Fe} = \emptyset^{a} \quad (2\text{-}63)$$

$$E_{corr} - E_{O_2} = \emptyset^{a} \quad (2\text{-}64)$$

According to Maekawa et al. (2009), the anodic Tafel gradient depends on temperature and chloride concentration, while they assumed a constant cathodic Tafel gradient equal to 0.14 through sensitivity analysis. They established several experimental tests to verify the effect of environmental conditions at the anodic controlled corrosion. They introduced the chloride-induced corrosion in concrete as the anodic controlled process. The anodic controlled process means corresponds to the conditions that the changes of the cathodic current density and half-cell potential due to environmental conditions (e.g. Temperature and chloride changes) are not considerable compared to the anodic site. However, the time transient ambient conditions and the chloride concentration impact the characteristics of the anode half-cell.

2.8.1 Effect of temperature on corrosion

Based on the Nernst's equation, the anodic Tafel gradient is raised when concrete temperature increases. The corrosion current density is reduced due to the increase in the anodic gradient slope. However, rising temperature leads to increasing the rate of corrosion in concrete. Maekawa (2009) used the Arrhenius's law to simulate the anodic current density, i_0^a as a function of temperature, as follows:

$$i_{0,T}^{a} = i_{0,Ts}^{a}.\exp\left(\frac{-\Delta E_a}{R}\left(\frac{1.0}{T} - \frac{1.0}{T_s}\right)\right) \quad (2\text{-}65)$$

where $i^{a}_{0,T}$ is the equilibrium exchange current density of the anodic site at an arbitrary temperature, T (K), and $i^{a}_{0,Ts}$ is the equilibrium exchange current density at the reference temperature, T_s. ΔE_a is the activation energy of the anodic reaction, where $\frac{\Delta E_a}{R}$ is equal to 1.5×10^{4}.

2.8.2 Effect of chloride on corrosion

Maekawa et al. (2009) expressed the following equation to model the effect of chloride on corrosion:

$$f_p = 3.17 \times 10^{-2}. C_f^{-1.04} \tag{2-66}$$

where C_f is the mass ratio of free chloride ions to the cement (%).They introduced the modified anodic Tafel slope as an empirical function of parameter f_p:

$$\beta_a = \left(\frac{2.303RT}{0.5Z_{Fe}F}\right). f_p \tag{2-67}$$

2.9 Linear modeling of the corrosion current density

The Tafel diagram consists of two straight lines in the anodic controlled corrosion, where the activation polarization is the dominant polarization term. Maekawa et al. (2009) calculated the corrosion current density, i_{corr} and corrosion potential at each time step of analysis by solving the linear equations, as follows:

$$i_{corr} = 10^{(E_{O_2} - E_{Fe} + \beta_a.\log(i^{a}_{0,T}) + \beta_c.\log(i^{c}_{0}))/(\beta_a + \beta_c)} \tag{2-68}$$

The final step in modeling of chloride-induced corrosion is calculating the loss of reinforcing steel thickness, X(t) during service life of concrete structures. Based on the Faraday's law, the loss of reinforcing steel thickness, X(t) is obtained, as follows:

$$X(t) = \frac{M}{Z_{Fe}.F.\rho_{Fe}} \int_0^t i_{corr}(t).dt \quad (2\text{-}69)$$

where M is the molecular mass of the iron ion (=55.845E-3 Kg/mol), F is Faraday's number (=9.65E+4 C/mol), Z_{Fe} is the number of charge of iron ions (=2), ρ_{Fe} is the steel density (=7.85E3 Kg/m^3) and i_{corr} (t) is the corrosion current density(A/m^2).

2.10 Discussions

In this research, a large numbers of studies on the modeling of the two different stages of corrosion in reinforced concrete structures is reviewed (Doa et al. 2010, Fish and Belytschko 2007, Hall and Hoff, 2012, Hansen and Saoumo 1999-a and b, Huang et al. 2015, Isgor and Ghani Razaqpur 2006, Kwon et al. 2009, Maekawa et al. 2009, Michel et al. 2013, Pour-ghaz et al. 2009). Based on the critically reviewed literature, explained in this chapter, the existing models for simulating the chloride-induced corrosion analysis can be improved more. Some of the critiques for further improvement are summarized as follows:

- Simplification of the complex ambient conditions, complicated interaction of different phases and various substances and the coupling effects of different with limited experimental calibrations is unrealistic

- Ignoring the simultaneous decoupled effects in both initiation and process of corrosion considering time-transient environmental parameters during the time-span of the concrete reduces the accuracy of analysis.

Nevertheless, all these attempts are valuable to improve the computational models of the scalar fields, including time-dependent thermal analysis, time-dependent moisture analysis, time-dependent chloride diffusion and advection analysis as well as solid mechanic analysis. In this research, the nonlinear finite element program, *VT-MultiPhys* is developed to simulate the chloride transport in concrete as the multi-physics phenomenon which is impacted by heat transfer, moisture flow and chloride transport in concrete. In next chapters, the methodology of the analysis program to simulate the influential physical parameters on chloride-induced corrosion including temperature, relative humidity and water content is described in detail. In addition, the methodology of finite element modeling of the physical parameter is supplemented by a set of verification analysis.

3 Methodology and analysis of heat transfer in concrete

This Chapter presents methodology and validation analyses for heat transfer in concrete. Most of the physical parameters in concrete such as water content, water liquid density, concrete viscosity and chloride diffusion coefficient are impacted by temperature. So, thermal analysis is a key analysis which should be performed to enable modeling of the coupled parameters.

3.1 Methodology of thermal analysis

The chloride transport in concrete and so the chloride-induced corrosion are impacted by the time-dependent distribution of temperature. In this research, the time-dependent distribution of temperature is obtained through the heat transfer analysis via the developed analysis program. The program is able to conduct nonlinear time- transient chloride diffusion analysis, while simultaneously it may compute the nodal temperatures, T (˚C), through linear steady state heat transfer analysis. Also, in general, concrete body can be modeled as a non-homogeneous and non-isotropic material in the developed finite element program. Concrete density and the specific heat of concrete are independent of temperature. The time-dependent spatially varied heat source, S(x,y,z,t) is defined as a time-dependent polynomial function. The heat source is positive when the heat supply is released due to the cement hydration or other chemical reactions within concrete, while it

could have negative sign if chemical reactions in the concrete absorb heat from the surrounding environment.

3.1.1 Modeling of thermal conductivity

Lienemann et al. (2005), introduced thermal conductivity as a polynomial function of temperature. In the analysis program, the maximum order of polynomial function is limited to one, as follows:

$$D(T) = a_0 + a_1 T \tag{3-1}$$

where a_0 and a_1 are constant coefficients of a polynomial function and T is temperature at each Gaussian points.

3.1.2 Modeling of heat flux at concrete surfaces

In the analysis program, the total heat flux at concrete surfaces, q (W/m^2.sec) is defined as the summation of convection flux, q_c , thermal irradiation flux, q_r and total absorbed radiation, q_s, which are introduced in the equations (2-18), (2-20) and (2-21), respectively. In this thesis, the effect of thermal irradiation flux and total absorbed radiation flux on the total heat flux is ignored.

3.2 Model description

The thermal analysis in this chapter is focused on the experimental tests conducted by Wang and Xi (2017) on prismatic concrete specimens subjected to different environmental

conditions. As shown in Figure 3.1, the two-dimensional finite element model is a 6 inch×12 inch (0.1524 m×0.3048 m) rectangle. The model consists of 242 nodes and 120 square four-node quadrilateral (4Q) elements, with the element size equal to 0.5 in. In accordance with the values adopted in Hansen and Saouma (1999a), concrete thermal conductivity, concrete density and heat capacity were set equal to 2.5613 W/m.°K, 2300 Kg/m^3 and 1170 J/(Kg.°K), respectively.

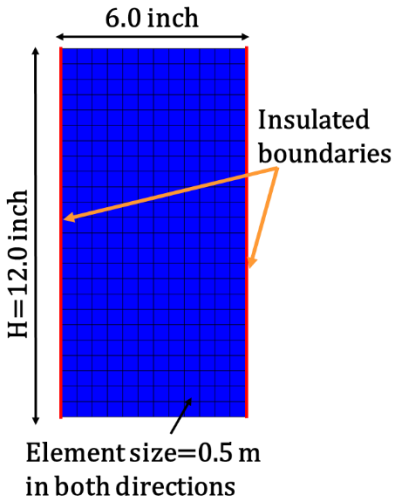

Figure 3.1: 2D finite element model in thermal analysis

In the experimental tests, the lateral surfaces of the specimen were insulated, so that heat inflow and outflow was only allowed from the top and bottom surfaces. The bottom concrete surface was directly exposed to the ambient temperature, which was constant and equal to the room temperature at initial time of analysis (=20°C), while the top surface was warmed by the controlled heater to reach the higher temperature than the initial value. The concrete specimens were cured for 28 days and then kept in the room temperature (=20°C) for 37 days to reach the uniform steady state condition before the experimental

tests began. It was assumed that the cement hydration was completed during the curing time. Therefore, the effect of heat released due to the cement hydration and so the heat source were ignored in the thermal analysis.

In order to model the boundary conditions in the thermal analysis, the constant essential boundary conditions are defined at the top surface, which is equal to the temperature produced by the controlled heater in the experimental tests. Since the bottom concrete surface is continuously exposed to the constant room temperature (=20°C), the boundary condition at the bottom surface is simplified to the constant essential boundary temperature.

A set of experimental tests, corresponding to different values of constant ambient temperature in the vicinity of top and bottom surfaces, were considered, as summarized in Table 3.1.

Table 3.1: Ambient temperature in the vicinity of the top and bottom surfaces for the experimental tests by Wang and Xi (2017)

Test	$T_{ambient}$ at bottom surface, °C	$T_{ambient}$ at top surface, °C
I-20	20	20
I-70	70	70
N-40	20	40
N-60	20	60
N-70	20	70

3.3 Analysis results and discussions

The typical distributions of temperature at time of 10 days obtained from the thermal analyses of test N-40, test N-60 and test N-70 are presented in Figures 3.2 to 3.4.

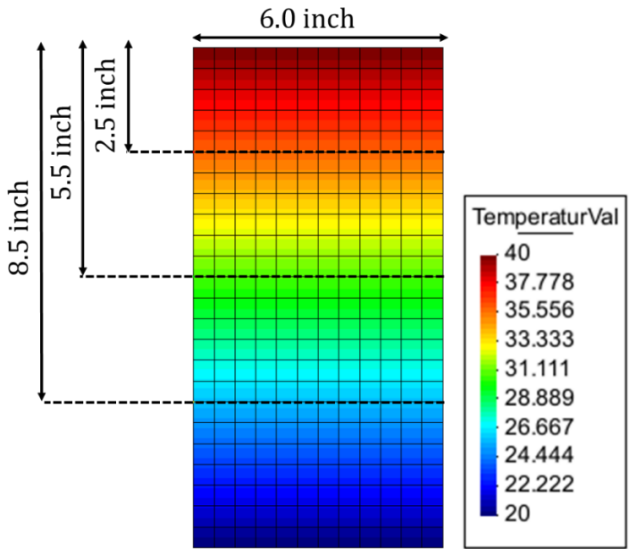

Figure 3.2: Analytically obtained temperature distribution at time of 10 days from thermal analysis of concrete model with geomentry and boundary conditions based on test N-40 by Wang and Xi (2017)

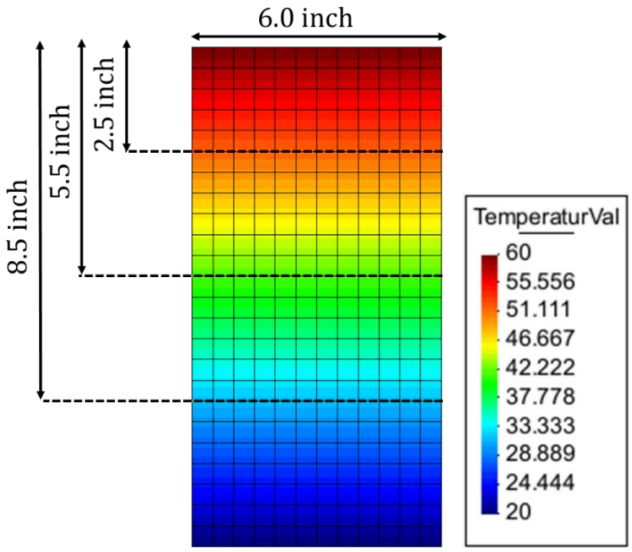

Figure 3.3: Analytically obtained temperature distribution at time of 10 days from thermal analysis of concrete model with geomentry and boundary conditions based on test N-60 by Wang and Xi (2017)

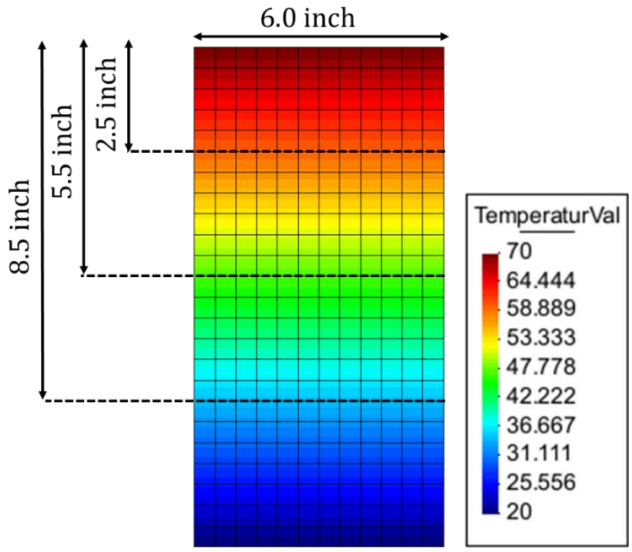

Figure 3.4: Analytically obtained temperature distribution at time of 10 days from thermal analysis of concrete model with geomentry and boundary conditions based on test N-70 by Wang and Xi (2017)

The comparison between the analytically obtained and experimentally recorded temperature distributions for the different tests, at a time of 10 days, is presented in Figure 3.5. It can be seen that the overall qualitative trend of the analysis results is similar to that

of the experimental data. However, the quantitative agreement is rather unsatisfactory. The disagreement between analytically obtained and experimentally recorded temperature values is attributed to the fact that the analysis results reach the steady-state temperature distribution much faster than in the experimental tests. For example, in test N-70, the temperature at different depths reached their steady state values at early stage of analysis, when time of 12.5hrs. The time history of thermal analysis results of test N-70 at three different depths are depicted in Figure 3.6.

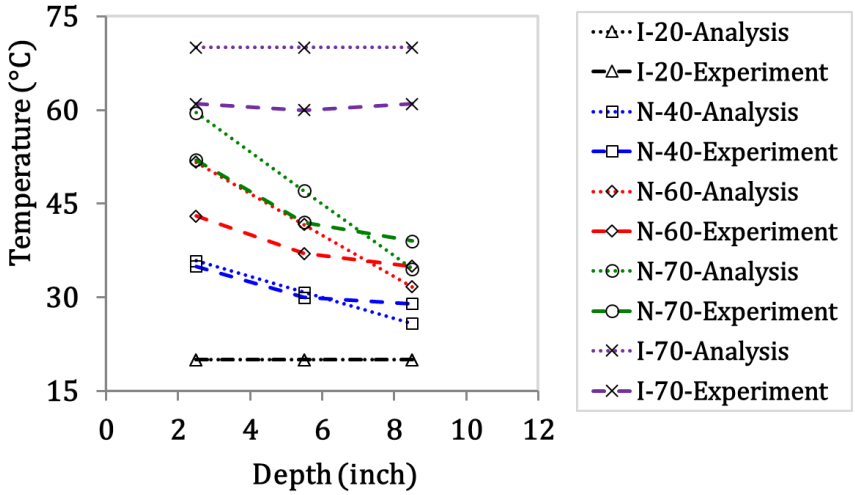

Figure 3.5: Comparison of temperature distributions for different boundary conditions at time of 10 days between the analytically obtained by the developed program and experimentally recorded by Wang and Xi (2017)

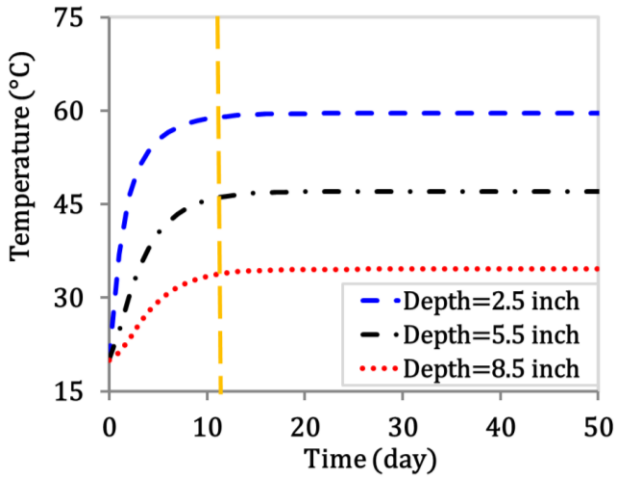

Figure 3.6: Time history of analytically obtained temperature from finite element thermal analysis of concrete model with geomentry and boundary conditions similar to test N-70 by Wang and Xi (2017)

3.4 Evaluation of thermal analysis methodology

A further set of analyses is conducted to evaluate the capability of finite element models to reproduce simple closed-form solutions. To this end, the temperature distribution of a semi-infinite, one-dimensional bar is considered. The left end is located at x = 0 and subjected to a surface temperature equal to T_s=20°C. The initial temperature at all other locations of the bar is equal to T_0 = 0°C. The temperature at a location, x at a time t is then given by the following expression.

$$T = T_0 + (T_s - T_0)(1 - \mathrm{erf}(z)) \tag{3-2}$$

where erf(z) is the error function of variable $z = \left(\frac{x}{2\sqrt{kt}}\right)$, and k is the constant parameter which depends on the thermal conductivity, specific heat capacity and concrete density as shown in Equation (3-3). The values of thermal conductivity, specific heat capacity and density are set equal to those adopted in the finite element thermal analyses.

$$K = D_T / C.\rho \quad (3\text{-}3)$$

Wang and Xi (2017) claimed that the temperature distributions in the experimental tests could be well captured by the closed-form solution of a semi-infinite bar. To verify that the proposed analysis program can reproduce the closed-form solution, a truncated model of a one-dimensional bar, subjected to a temperature of 20°C at one of the two ends was analyzed. The bar was truncated at the location x = 12 in. The initial temperature of the bar was equal to zero, and the other end of the bar had a generalized natural boundary condition. The ambient temperature at the generalized natural boundary was equal to 0°C, and the natural boundary coefficient was set equal to h_c = 2W/(m^2K). As shown in Figure 3.7, the specific natural boundary coefficient simulate the impact of the truncated portion of the semi-infinite bar. In Figure 3.8, it is shown how by modeling the impact of the truncated portion of the semi-infinite bar, the finite element model can accurately reproduce the closed-form solution.

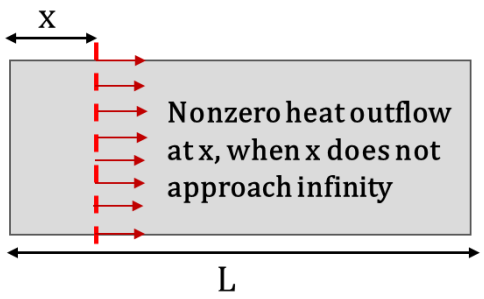

Figure 3.7: Schematic illustration of the heat outflow at section x to simulate the impact of the truncated portion of semi-infinite bar

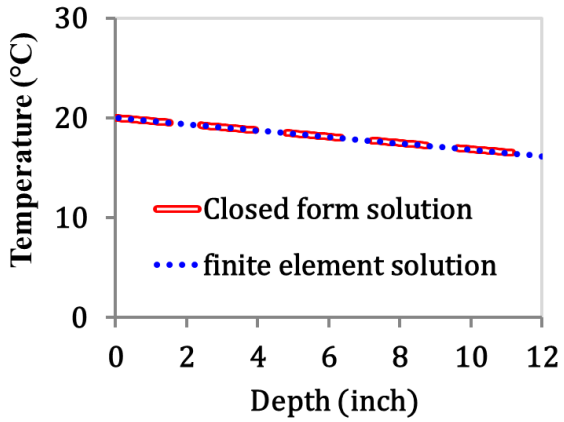

Figure 3.8: Verification of the analytically obtained temperature of the concrete model with the same geometry to the experimental specimens by Wang and Xi (2017) which is exposed to T=20°C at top surface and the nonzero heat outflow (hc = 2W/m2.K) at the bottom surface with the closed form solution

The closed-form solution was then used to estimate the experimentally recorded temperature distributions in the tests by Wang and Xi (2017). As shown in Figure 3.9, where the comparison between the closed-form solution and the experimental observations is provided for test N-70, the error-function solution cannot match the experimental data. This may be due to the fact that the values of conductivity and heat capacity in the concrete used by Wang and Xi (2017) were significantly different than those proposed by Hansen and Saouma (1997a). Still, a review of the literature indicates that the adopted material parameters in heat transfer analysis of concrete have not been assigned values much different than those adopted herein. Thus, it may be more meaningful to pursue validation analyses using experimental tests other than those of Wang and Xi (2017).

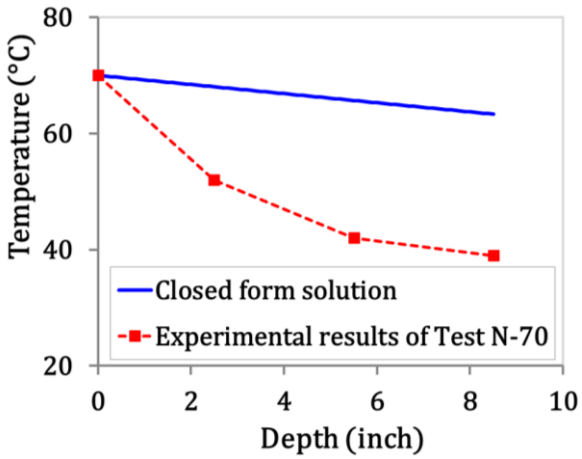

Figure 3.9: Comparison of the closed form solution and experimentally recorded temperature of the test N-70 by Wang and Xi (2017) at time of 10days

4 Methodology and analysis of moisture transport in concrete

This Chapter presents methodology and validation analyses of moisture transport in concrete. Water plays an important role in the initiation and process of chloride-induce corrosion. Wet concrete facilitates the electron transfer from anodic to cathodic sites in the electrochemical cells. Also, chloride diffusion and advection depend on the water content in concrete. The analysis program simulates the concrete body where the liquid and vapor phases of water can be transported. Water velocity is the other parameter which is computed by the analysis program. The velocity of water flow in concrete is the key parameter to estimate the contribution of advective force to the transport of chemical substances.

4.1 Methodology of moisture transport analysis

Water content in concrete is impacted by temperature distribution. In the analysis program, moisture transport analysis is followed by thermal analysis. Therefore, water content in concrete can be determined as the implicit function of temperature, which is obtained by thermal analysis. Also, the analysis program is able to simplify the coupling effect of thermal analysis on moisture transport analysis by assuming the time-dependent uniform distribution of temperature in concrete body.

4.1.1 Modeling of concrete body

Concrete body is assumed as a homogeneous and isotropic material. Concrete density, ρ_L is defined by equation (2-26), which was proposed by Maekawa et al. (2009). The paste porosity, $\emptyset_{Paste}$ and the total concrete porosity are determined by equations (2-41) and (2-42), respectively, where the volume fraction of small and large capillary pores, gel pores and interlayer pores should be defined as input parameters. The moisture characteristics of concrete pore channels including moisture capacity and moisture conductivity are determined as the nonlinear functions of capillary pore pressure at each Gaussian point. Capillary pore pressure is initialized at the beginning of moisture transport analysis. The nonlinearity in concrete characteristics render the nonlinear moisture transport analysis.

4.1.1.1 Modeling of moisture capacity

As proposed in equation (2-24), by using the Chain rule, moisture capacity, α_P can be determined as an implicit function of total capillary pressure, P_c; relative humidity, h; total saturation degree of concrete, S_{Total}; and water content in concrete pore channels, θ_w. The algorithm in the analysis program to calculate moisture capacity, α_P at each Gaussian point is summarized in Figure 4.1. In this research, capillary pressure, P_c is the main scalar physical field parameter in moisture transport analysis. As shown in equation (2-27), relative humidity at each Gaussian point is obtained based on Kelvin's law.

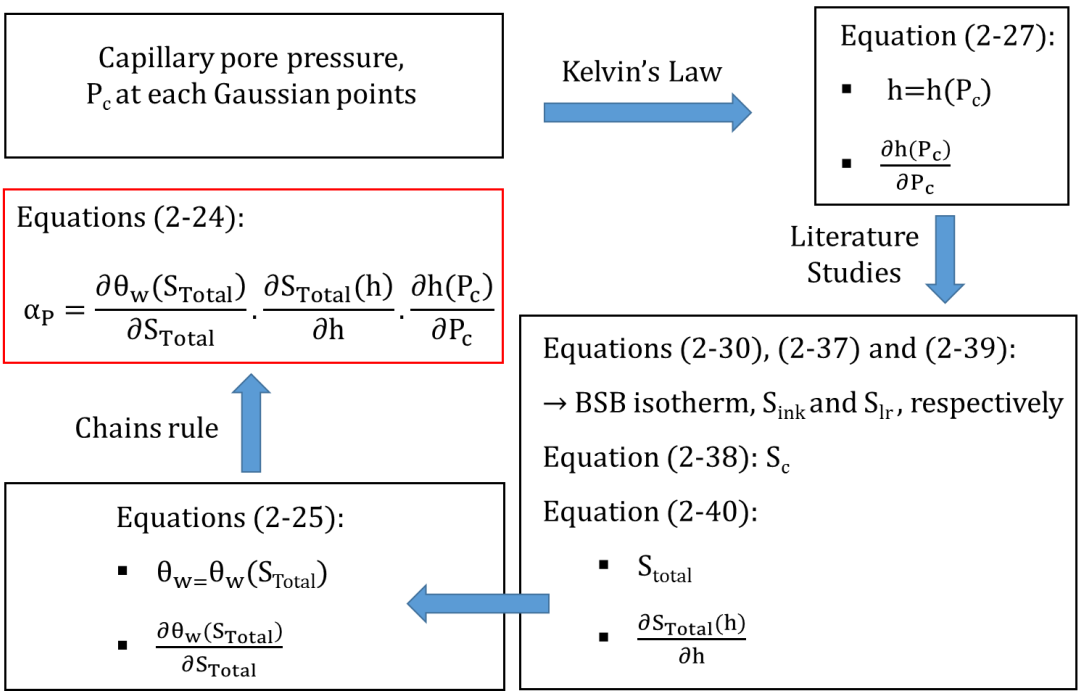

Figure 4.1: Schematic illustration of the algorithm to calculate the concrete moisture capacity, α_P

In the analysis program, the moisture behavior in concrete is precisely simulated by BSB isotherm, ink-bottle isotherm, S_{ink} and interlayer isotherm, S_{lr}. The effect of condensed water in capillary and gel pores is calculated by the BSB moisture isotherm which is presented in equation (2-30), while the hysteresis behavior of condensed moisture isotherm due to the ink-bottle effect, S_{ink} is modeled by the empirical equation (2-37) which was introduced by Maekawa et al. (2009). Using equation (2-38), saturation degree due to the condensed water, S_c is calculated as the summation of BSB isotherm and ink-bottle isotherm. The hysteresis effect of water in interlayer pores, S_{lr} is modeled by equation (2-39) which was proposed by Maekawa et al. (2009). In equation (2-40), the contribution of condensed water and interlayer isotherm to the total saturation degree at each Gaussian points, S_{Total} is determined. In accordance with the equation (2-25), total

water content, θ_w at each Gaussian points, is a linear function of total saturation degree. As proposed in equation (2-24), the parameter α_P is mathematically obtained by using the Chain rule.

4.1.1.2 Modeling of moisture conductivity

In this research, as proposed in equation (2-43), the macroscopic moisture conductivity of concrete, D_P is defined as the summation of conductivity of liquid water, K_L and water vapor, K_V.

According to Hall and Hoff, (2012), the horizontal capillary flow of liquid water, u_x, depends on the gradient of $(S_{Total} \times \text{Porosity})$, as follows:

$$u_x = -D(\theta_w).\frac{d(S_{Total}\times \text{Porosity})}{dx} \tag{4-1}$$

Also, Hall and Hoff, (2012) modeled the liquid diffusion coefficient, $D(\theta_w)$ by the following empirical formulation:

$$D(\theta_w) = D_0.\exp(B.\text{Porosity}.S_{Total}) \tag{4-2}$$

where B and D_0 are the constant parameters, which are calibrated based on material characteristics. Plugging equations (2-25) and (4-2) into the equation (4-1) and using the Chain rule, the equation (4-3) is concluded, as follows:

$$u_x = -D_0.\exp(B.\text{Porosity}.S_{Total}).\left\{\frac{d(\text{Porosity}.S_{Total})}{dh}.\frac{dh}{dP_c}.\frac{dP_c}{dx}\right\} \tag{4-3}$$

Hall and Hoff, (2012), suggested $B \times \text{Porosity}$ is equal to seven for concrete material. Therefore, the liquid conductivity parameter, K_L, is calculated, as follows:

$$K_L = D_0 . \exp(7 \times S_{Total}) . \text{Porosity} . \left\{ \frac{d(S_{Total})}{dh} . \frac{h . M_w}{\rho_L R_g T} \right\} \quad (4\text{-}4)$$

In this research, the water vapor flux, J_w is obtained based on the Fick's linear law, as follows:

$$J_w = - \frac{D_w M_w}{R_g T} . \frac{dp_v}{dx} \quad (4\text{-}5)$$

where D_w is the vapor diffusivity (m^2/T). Based on the equal Gibb's free energy in both liquid and gaseous phases of water, the water vapor pressure, p_v is defined as the linear function of relative humidity, h; and the saturated water vapor pressure, $p_{v,sat}$ (Maekawa et al. 2009); as follows:

$$p_v = h \times p_{v,sat} \quad (4\text{-}6)$$

using the Clausius-Clapeeyron equation which was proposed by Maekawa et al. (2009), the $p_{v,sat}$ is defined by the following equation:

$$p_{v,sat} = p_0 . \exp \left\{ - \left(\frac{\Delta H_{vap}}{R_g} \right) \left(\frac{1}{T} - \frac{1}{T_0} \right) \right\} \quad (4\text{-}7)$$

where ΔH_{vap} is the heat of evaporation (KJ/mol), while p_0 and T_0 are the pressure and temperature at the reference condition, respectively. Using the Chains rule, J_w can be obtained by equation (4-8).

$$J_w = -\frac{D_w M_w}{R_g T} \cdot \left\{ \frac{dp_v}{dh} \cdot \frac{dh}{dP_c} \cdot \frac{dP_c}{dx} \right\} = -K_v \cdot \frac{dP_c}{dx} \tag{4-8}$$

where K_v is the vapor diffusion coefficient, which is calculated by plugging the equations (4-6) and (4-7) into the equation (4-8). The term $(1 - S_{Total})$ in the equation (4-9) guarantees no vapor transfer in the saturated concrete.

$$K_v = \frac{D_w \cdot p_{v,sat}}{\rho_L} h. (1 - S_{Total}). \left(\frac{M_w}{R_g T} \right)^2 \tag{4-9}$$

4.1.2 Modeling of moisture flux at concrete surfaces

As shown in equation (2-44), Maekawa et al. (2009) proposed an empirical equation to simulate the generalized boundary conditions in moisture transport analysis. In the analysis program, equation (2-44) was implemented to model the moisture flux at concrete surfaces, while the emissivity coefficient, E_b was calibrated to 3 E-5.

4.2 Model description

The moisture transport analysis in this chapter is focused on the experimental tests conducted by Wang and Xi (2017) on the similar prismatic concrete specimens which were described in Figure 3.1. In the experimental tests, the lateral surfaces of the specimen were insulated, so that moisture inflow and outflow was only allowed from the top and

bottom surfaces. The bottom concrete surface was directly exposed to the ambient with 50% relative humidity, which is equivalent to uniform capillary pore pressure of -9.33E7 Pa. The top surface of concrete was completely submerged during the experimental tests to guarantee the 100% relative humidity at the top boundary. Boundary conditions at concrete surfaces for different tests are summarized in Table 4.1.

Table 4.1: Ambient temperature and relative humidity in the vicinity of the top and bottom surfaces for the experimental tests by Wang and Xi (2017)

Test	$T_{ambient}$ at bottom surface, °C	$T_{ambient}$ at top surface, °C	$h_{ambient}$ at bottom surface, %	$h_{ambient}$ at top surface, %
I-20	20	20	50	100
I-70	70	70	50	100
N-40	20	40	50	100
N-60	20	60	50	100
N-70	20	70	50	100

The concrete specimens were cured for 28 days and then kept in the room condition with 50% ambient relative humidity to reach the uniform steady state condition before the experimental tests began. The rate of loss of moisture in concrete specimens, Q_P can be affected by cement hydration. It was assumed that the cement hydration of concrete specimens was completed during the curing time. Therefore, in the absence of chemical reactions inside concrete body, Q_P is equal to zero after the completion of cement hydration.

In this research, moisture transport analysis was coupled with thermal analysis. In accordance with the thermal analysis in chapter 3, similar values were adopted for concrete thermal conductivity, concrete density, heat capacity and heat flux. In Table 4.2, the concrete material properties for the coupled moisture transport analysis are presented.

Table 4.2: Concrete material properties for the moisture transport analysis

Thermal Characteristics	Conductivity (W/m.°K)	2.5613
	Concrete density (Kg/m^3)	2300
	Heat capacity (J/Kg.°K)	1170
Moisture Characteristics	Porosity due to the large capillary pores	0.12068
	Porosity due to the small capillary pores	0.11872
	Porosity due to the gel pores	0.03752
	Porosity due to the microscopic pores	0.00308
	KL_0	1.00E-06
	KV_0	1.00E-06
	Curing time (day)	28
	Water to Cement ratio	0.6
	Cement type	I
	Emmisivity coefficient	3.00E-05

4.3 Analysis results and discussions

The analytically obtained distributions of relative humidity for the different tests, at a time of 10 days, is presented in Figure 4.2.

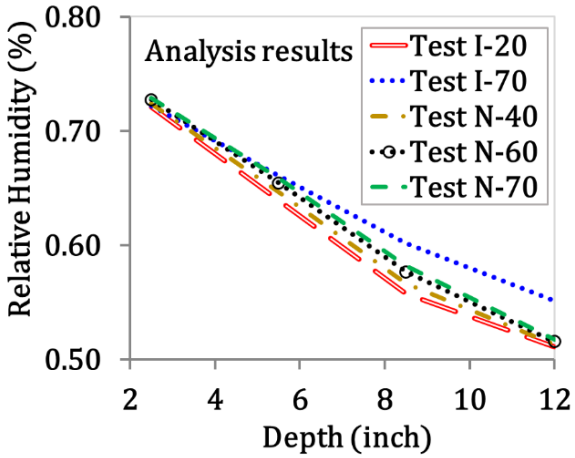

Figure 4.2: Analytically obtained distributions of relative humidity along the height of concrete model at time of 10 days from finite element moisture transport analysis of concrete model with geomentry and boundary conditions based on the experimental tests test by Wang and Xi (2017)

It can be seen that the relative humidity at depth of 2.5m in different tests is almost similar. The qualitative trend of the analytical results is rather unsatisfactory. Although the elevated relative humidity is expected due to the temperature growth inside the concrete body, the analytical solution of the coupled moisture analysis showed no sensitivity to the temperature changes. The disagreement between analytically obtained and real physical behavior is attributed to the fact that in wetting condition, the total saturation degree of concrete pores is obtained by the BSB isotherm, which is the function of relative humidity and temperature. The contribution of the hysteresis moisture isotherms, S_{ink} and S_{lr}, to the total saturation degree is ignored in the wetting condition.

As shown in Figure 4.3, the sensitivity of the BSB isotherm to increase in temperature from 20°C to 60°C is negligible.

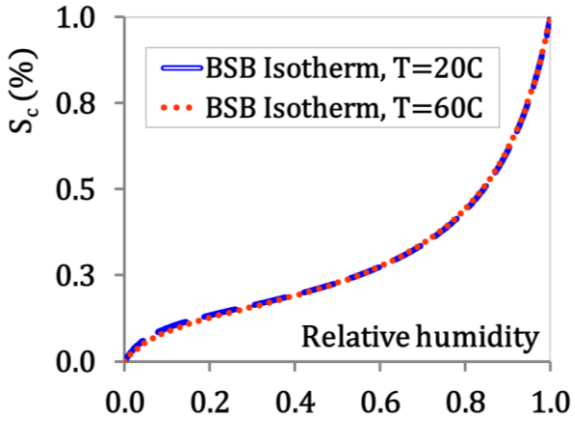

Figure 4.3: Schematic illustration of sensitivity of the BSB isotherm to the increase in temperature from 20°C to 60°C

In this research, two numerical equations were introduced to capture the sensitivity of the coupled moisture transport analysis to temperature during wetting stage. The equations (4-10) and (4-11) are introduced as a practical solution to precisely simulate the coupling effect of thermal analysis on moisture transport analysis. The accuracy of these equations should be evaluated based on more reliable experimental documents.

$$D_p = D_p . \exp(-\frac{\text{Temperature}}{200.0}) \quad (4\text{-}10)$$

$$\alpha_P = \alpha_P . \exp(-\frac{\text{Temperature}}{250.0}) \quad (4\text{-}11)$$

where D_p is the macroscopic moisture conductivity of concrete and α_P is the amount of released or absorbed water fraction volume per a unit change of capillary pressure. The

modified distribution of relative humidity along the height of concrete models is illustrated in Figure 4.4.

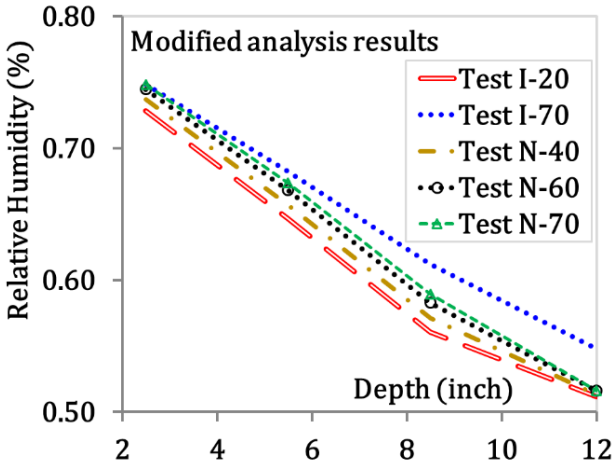

Figure 4.4: Analytically obtained distributions of modified relative humidity along the height of concrete model at time of 10 days from finite element moisture transport analysis of concrete model with geomentry and boundary conditions based on the experimental tests test by Wang and Xi (2017)

Figure 4.4 shows that the modified parameters successfully simulated the sensitivity of moisture transport analysis to the increase in temperature. In test I-70 where concrete experienced the highest temperature distribution of 70°C, concrete has the maximum relative humidity at depth of 2.5 m, while, the minimum relative humidity corresponds to the test I-20, where the concrete has the least temperature distribution.

4.4 Validation of moisture transport analysis methodology

As discussed in the previous chapter, the values of thermal conductivity and heat capacity in the concrete used by Wang and Xi (2017) were significantly different than the adopted material parameters in heat transfer analysis of concrete. The difference between

the analytically obtained and experimentally recorded temperature distributions influences the coupled moisture transport analysis. If temperature distributes uniformly in concrete, moisture transport analysis can be modeled decoupled from thermal analysis. In test I-20, the uniform distribution of temperature remained constant during analysis time. As shown in Figure 4.5, the overall qualitative and quantitative trends of the analysis results are similar to that of the experimental data.

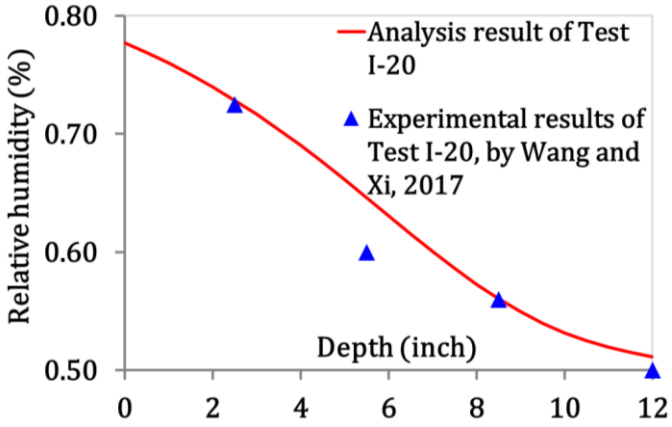

Figure 4.5: Comparison between the analytically obtained from the developed program and experimental results by Wang and Xi (2017) for relative humidity distributions of the test I-20 at time of 10 days

In Figure 4.6, the time history of relative humidity at different depths of concrete specimen for the test I-20 is shown. It can be observed that in spite of quick convergence to the steady state condition in thermal analysis, the small moisture diffusion coefficient of concrete, postponed the convergence in the moisture transport analysis.

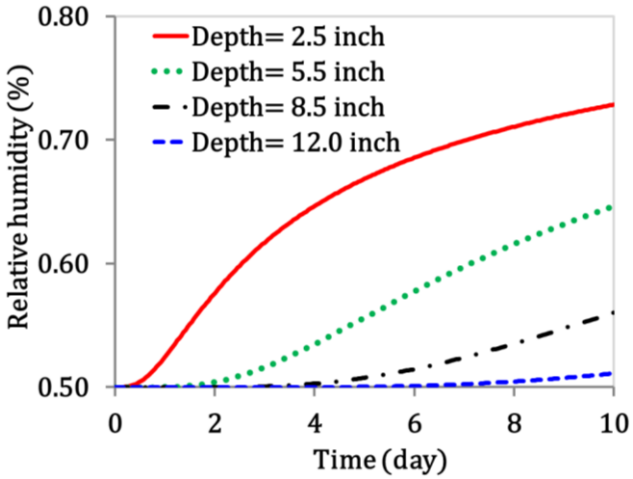

Figure 4.6: Analytically obtained time history of relative humidity at different depths from finite element moisture transport analysis of concrete model with geomentry and boundary conditions based on the experimental tests I-20 by Wang and Xi (2017)

4.5 Parametric analysis

In this research, the sensitivity of moisture transport analysis to the curing time of concrete, water to cement ratio and the characteristics of cement paste are studied. Also, the contribution of hysteretic moisture isotherms, S_{ink} and S_{lr}; to the analytically obtained distribution of relative humidity is studied.

4.5.1 Effect of curing time

During wetting condition, condensed saturation degree, S_c is obtained by the BSB moisture isotherm. The effect of curing time of concrete on the condensed saturation degree, S_c is studied for test I-20. As shown in Figure 4.7, during the wetting stage, the contribution of the condensed phase of pore water is elevated by increasing the curing time of concrete. The required curing time of concrete depends on several factors such as the mixture proportion of concrete and environmental exposure conditions at concrete

surfaces. By increasing the curing time of concrete, the required moisture to continue the cement hydration is provided by the external ambient source. Therefore, the loss of interior moisture content of concrete due to the cement hydration is significantly reduced.

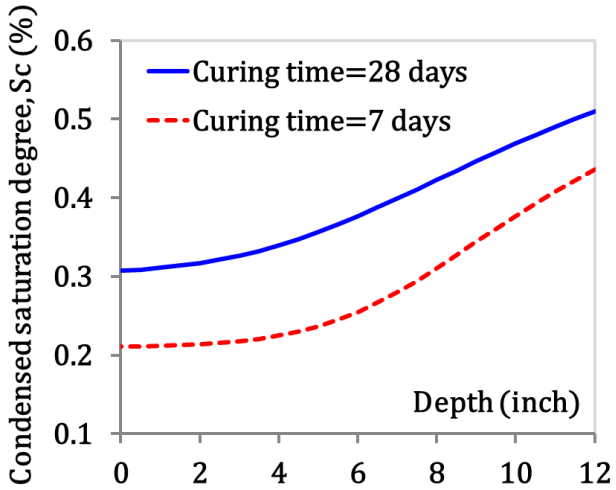

Figure 4.7: Effect of time curing on the analytivally obtained condensed saturation degree for the concrete model with geomentry and boundary conditions based on the experimental tests I-20 by Wang and Xi (2017)

4.5.2 Effect of cement type

As proposed in equation (2-35), Xi et al. (1994) calibrated the parameter N_{ct} (C_t) to simulate the effect of cement type, C_t on moisture isotherm behavior of concrete. The parameter N_{ct} has been calibrated for different cement types, based on the percentage of major compounds and fineness of cement (Mokarem, 2017), which control the amount and rate of hydration process and loss of moisture in concrete. As shown in Figure 4.8, by increasing the parameter N_{ct}, the condensed saturation degree, S_c and so the contribution of the capillary and gel pores to the total saturation degree would be reduced.

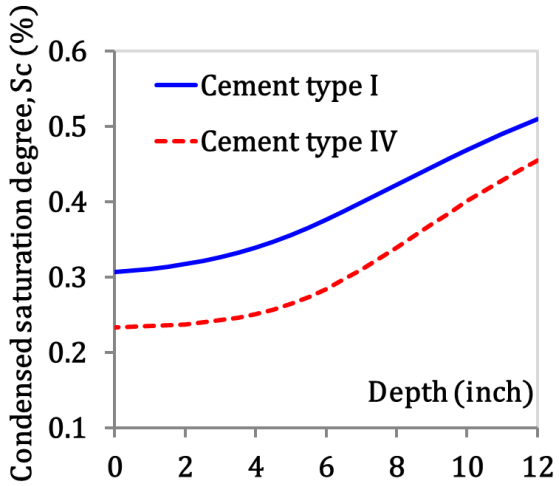

Figure 4.8: Effect of cement type on the analytivally obtained condensed saturation degree for the concrete model with geomentry and boundary conditions based on the experimental tests I-20 by Wang and Xi (2017)

4.5.3 Effect of water to cement ratio

As shown in Figure 4.9, the analysis program can successfully capture the effect of water to cement ratio on the condensed saturation degree, S_c. The increase in water to cement ratio results in rise in S_c and so the total water content in concrete body.

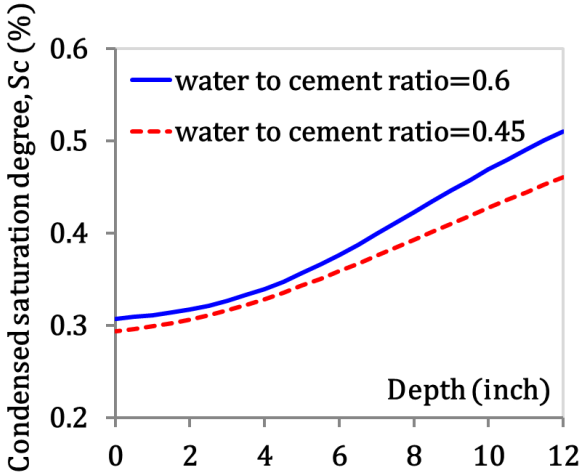

Figure 4.9: Effect of water to cement ratio on the analytivally obtained condensed saturation degree for the concrete model with geomentry and boundary conditions based on the experimental tests I-20 by Wang and Xi (2017)

4.5.4 Effect of the hysteresis behavior of moisture isotherms

In the absence of hysteresis effects during wetting stage, total saturation degree is equal to the condensed saturation degree which is obtained by the BSS isotherm. While, the total moisture content in concrete is significantly influenced by the hysteresis moisture isotherms during a drying condition. In the analysis program, the hysteresis behavior of the trapped water and interlayer water during the drying stage were simulated based on the proposed equations by Maekawa et al. (2009). This section is focused on the effect of hysteretic moisture isotherms on the analytically obtained relative humidity of concrete subjected to drying condition. The two-dimensional finite element model which is 0.01m ×4m rectangle was studied. The model consists of 802 nodes and 400 square four-node quadrilateral (4Q) elements, with the element size of 0.01 m. In accordance with the values adopted in test I-20, water to cement ratio, cement type and curing time were set equal to 0.6, III and 28days, respectively. The lateral surfaces of the concrete model were insulated. The initial interior relative humidity was set to 50%. In order to simulate the boundary conditions, it was assumed that the bottom concrete surface experienced constant ambient relative humidity equal to 50%. While, the top surface lost the initial water to reach relative humidity of 20%. The constant temperature of 50°C was assumed to be uniformly distributed in concrete body during analysis time. In Figure 4.10, the effect of hysteresis behavior of moisture isotherms on the analytically obtained relative humidity distribution is presented.

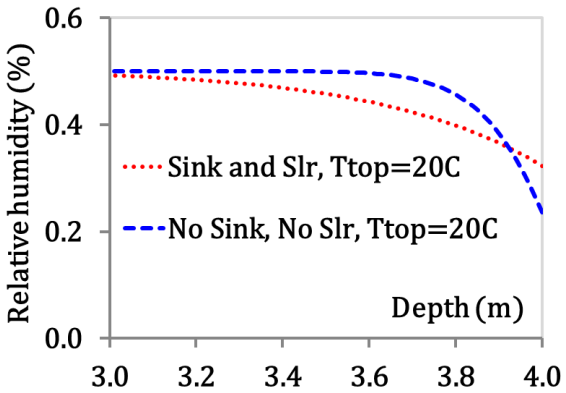

Figure 4.10: Effect of hysteretic moisture isotherms on the analytically obtained relative humidity distribution of the concrete model with geomentry and boundary conditions based on the experimental tests I-20 by Wang and Xi (2017)

It can be seen that the hysteretic moisture isotherms alter the distribution of relative humidity along the height of concrete. Therefore, the water trapped and the interlayer water in concrete should be precisely simulated during drying conditions. The sensitivity of total saturation degree at the virgin drying stage to the increase in temperature should be verified. In order to simulate the coupling effect of temperature on the moisture transport analysis during the drying stage or hysteresis cycles of wetting–drying, Maekawa et al. (2009) proposed the modified experimental equations for the hysteresis isotherms, S_{ink} and S_{lr}. Due to the lack of supplementary documents, the modified formulation have not been implemented in this research. But, there is still a room to improve the accuracy of moisture isotherms to capture the sensitivity of moisture analysis to temperature change.

5 Methodology and analysis of chloride diffusion in concrete

This Chapter presents methodology and validation analyses for chloride diffusion in concrete. Chloride transport in concrete is a complex multi-physics phenomenon which is impacted by several parameters, such as the coupling effects of the ambient heat and moisture transfer through concrete surfaces; diffusion path characteristics; crack propagation and stress distribution. The analysis program is able to quantitatively predict how the chloride diffusion in concrete depends on concrete characteristics and ambient conditions. Depassivation is the first consequence of chloride accumulation along steel bars in concrete. Chloride-induced corrosion initiates immediately after depassivation of the protective layer around steel bars. Since chloride ions contribute to the initiation of corrosion and corrosion process, chloride content in concrete should be precisely monitored during the life span of concrete structures.

5.1 Methodology of chloride diffusion analysis

Several parameters such as concrete mixture, interaction of pore wall structures and chloride ions, characteristics of diffusion path and binding chloride; affect the chloride diffusion coefficient, D_{Cl}. In addition, chloride diffusion coefficient is influenced by temperature distribution, water content and crack propagation in concrete. In the analysis program, the characteristics of concrete pore channels, where chloride ions transport are

simulated by introducing chloride diffusion coefficient as an implicit function of influential parameters, as follow:

$$D_{Cl} = f_1\left(T, S_{avg}, \Phi_{paste}, \Omega_{cp}, \delta_{cp}, C_f, C_b\right).\ f_2(w_{cr}) \quad (5\text{-}1)$$

where T is the analytically obtained temperature from thermal analysis, S_{avg} is the average of total saturation degree which is obtained by moisture transport analysis, as follows:

$$S_{avg} = \frac{S_{Total}(t_i)+S_{Total}(t_{i-1})}{2} \quad (5\text{-}2)$$

the analysis program is able to store the time-history of total saturation degree during time of analysis, so that $S_{Total}(t_i)$ is the total saturation degree at the current time step, t_i and $S_{Total}(t_{i-1})$ is the total saturation degree at the previous time step of analysis, t_{i-1}.

Ω_{cp} is the tortuosity, δ_{cp} is the constrictivity of the concrete, and C_f and C_b are the free chloride and binding chloride terms, respectively. The crack width of the concrete, w_{cr} is obtained by concrete stress distribution analysis. The coupled effects of thermal analysis and moisture transport analysis on chloride diffusion coefficient can be simplified to the time-dependent temperature and total saturation degree, respectively, which are uniformly distributed in concrete body during the analysis time.

5.1.1 Modeling of binding chloride

After the protective layer of steel bars depassivates, the binding chlorides may actively participate in the chloride transport during the chloride-induced corrosion process. In the

analysis program, the nonlinear experimental model proposed by Maekawa et al. (2009) has been implemented to simulate the binding chloride effect on the chloride transport. As shown in equation (5-3), Maekawa et al. (2009) introduced the binding chloride capacity based on the free chloride ions in concrete, C_f.

$$C_b = \frac{\alpha . C_f}{(1.0+4.0 C_f)} \tag{5-3}$$

where C_f and C_b are the mass ratio of free chloride ions to the cement and binding chlorides to the cement mass (%), respectively. The parameter α expresses the effects of mineral composition, cement admixture and replacement ratio of cement material, as shown in equation (5-4):

$$\alpha = \begin{cases} 11.8 & \text{Ordinary Portland Cement (OPC)} \\ -34.0b^2 + 23.3b + 11.8 & \text{Blast Furnace Slag (BFS)} \\ -15.5f^2 + 1.8f + 11.8 & \text{Fly Ash (FA)} \end{cases} \tag{5-4}$$

where b and f are the experimental parameters to express the replacement ratios by mass of cement additives. In the analysis program, chloride concentration, C_{Cl} (mol/m^3) is converted to C_f (% by mass of binder), as follows:

$$C_f = \frac{C_{Cl} . M_{Cl} . \emptyset}{\rho_{concrete} . C_{f,factor}} \times 100 \tag{5-5}$$

where M_{Cl} is the molecular mass of chloride ion (=35.453E-3 Kg/mol) and $\rho_{concrete}$ is the concrete density (Kg/m^3). According to Maekawa et al. (2009), $C_{f,factor}$ is defined as the ratio of cement mass to summation of cement, bound water and fine aggregate, as follows:

$$C_{f,factor} = \frac{W_{cement}}{W_{cement}+W_{bound\ water}+W_{fine\ aggregate}} \quad (5\text{-}6)$$

where, W_{cement}, $W_{bound\ water}$ and $W_{fine\ aggregate}$ are mass of cement, bound water and the fine aggregates, respectively, per unit volume of concrete (Kg/m^3).

The analysis program is able to compute the contribution of free chloride ions to the total chloride content in concrete. Also, the program implemented the proposed nonlinear model of chloride binding to calculate the binding chloride, C_b at each Gaussian points. Finally, total chloride concentration (% by mass of binder) is obtained as the summation of C_f and C_b.

5.1.2 Modeling of diffusion path characteristics

In the analysis program, the effect of concrete pore network on chloride diffusion is computationally modeled by three parameters: porosity, $\emptyset_{paste}$; tortuosity, Ω_{cp}; and constrictivity, δ_{cp}. Maekawa et al. (2009) proposed empirical equations to computationally simulate the characteristics of concrete pore channels. Theses equations have been implemented in this research. According to Maekawa et al. (2009), since chloride ions diffuse only through capillary and gel pores, the effective porosity to illustrate the diffusion path characteristics is the summation of capillary and gel porosity, $\emptyset_{paste}$ which is obtained by equation (2-41). Tortuosity of concrete pore channels, Ω_{cp}, is a function of concrete paste porosity, $\emptyset_{paste}$, as follows:

$$\Omega_{cp} = -1.5 \tanh\left(8.0\left(\emptyset_{paste} - 0.25\right)\right) + 2.5 \quad (5\text{-}7)$$

As shown in equations (5-8) to (5-10), Maekawa et al. (2009) introduced constrictivity, δ_{cp} as a function of pore microstructures and binding chloride.

$$\delta_{cp} = m.\delta_1.\delta_2 \tag{5-8}$$

$$\delta_1 = 0.495\tanh\{4.0(\log(r_{cp}^{peak}) + 6.2)\} + 0.505 \tag{5-9}$$

$$\delta_2 = 1.0 - 0.627C_b + 0.107C_b^2 \tag{5-10}$$

where m, δ_1 and δ_2 are the empirical parameters (Maekawa et al, 2009 and Maruya et al, 1995). In the analysis program, parameter m has been calibrated to unity. Parameter δ_1 simulates the contribution of radius size of capillary pores to chloride ion diffusion through concrete pore channels. As shown in equation (5-9), the increase in the maximum radius size of capillary pores, r_{cp}^{peak} (m), results in increasing parameter δ_1 and so constrictivity, δ_{cp}. The effect of binding chloride on the interaction of free chloride ions and pore wall structures is schematically illustrated in Figure 5.1.

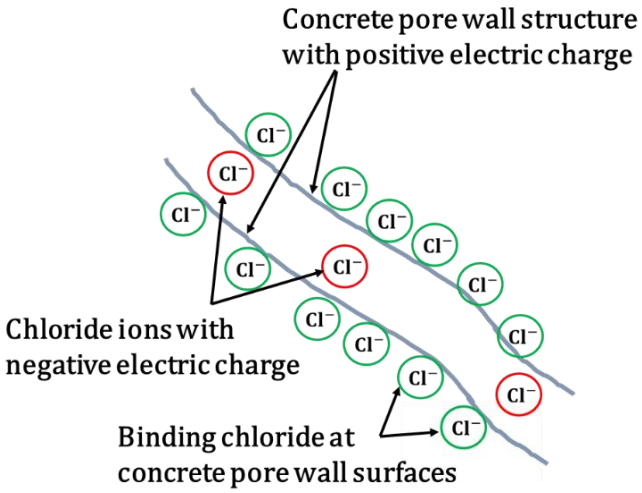

Figure 5.1: Schematic illustration of the binding chloride effect on diffusion of free chloride ions through concrete pore channnels

It can be observed that due to the accumulation of binding chloride with negative electric charge at concrete channels, the positive electric charge of pore wall structures would be neutralized. Also, the binding chloride disperse the other negatively charged chloride components, such as free chloride ions which try to diffuse through pore channels. Therefore, increasing the binding chloride in concrete results in a reduction in free chloride diffusion. In the analysis program, the effect of binding chloride on concrete constrictivity has been quantitatively simulated by equation (5-10).

5.1.3 Modeling of chloride diffusion coefficient

In the analysis program, the chloride diffusion coefficient, D_{Cl} (m^2/sec), is calculated based on Einstein's theorem, as follows:

$$D_{Cl} = R_g T \frac{\lambda_{ion}}{Z_{Cl}^2 F^2} \tag{5-11}$$

where R_g is the gas constant (=8.31447 J/mol.K); T is the time-transient temperature at each Gaussian points (˚K); λ_{ion} is the ion conductivity (S.m^2/mol); Z_{Cl} is the electric charge of chloride ions (=1); and F is Faraday's number (=9.65E+4 C/mol). Using Arrhenius's law, the coupling effect of temperature on the ion conductivity parameter, λ_{ion} , has been modeled by the following equation:

$$\lambda_{ion} = \lambda_{25} \exp\left[\frac{-E_a}{R}\left(\frac{1}{T} - \frac{1}{298.0}\right)\right] \quad (5\text{-}12)$$

where E_a is the activation energy of chloride ions (=17.6d3 J/mol) and λ_{25} is the reference chloride ion conductivity at a temperature of 25˚C (T_0= 298˚K). Finally, the chloride diffusion coefficient, $D_{Cl,diff}$ (m^2/sec), in the analysis program is obtained, as follows:

$$D_{Cl,diff} = \frac{Porosity.S_{avg}}{\Omega_{cp}} \delta_{cp} D_{Cl} \quad (5\text{-}13)$$

5.1.4 Modeling of chloride diffusion in cracked concrete

In the analysis program, the cracks are idealized to the open channels in concrete, where chloride ions can transport. In order to simulate the diffusion path in cracked concrete, the increment in the chloride diffusion coefficient is simulated by implementing the proposed crack function, f_{crack} by Known et al. (2009) as shown in equations (2-45) and (2-46). The analysis program is able to calculate the concrete tensile stress distribution, concrete propagation and concrete crack width during the analysis time. At each Gaussian point, the chloride diffusion coefficient increases if the crack width, w_{crack} (mm) exceeds the threshold value.

5.1.5 Modeling of chloride flux at concrete surfaces

In the analysis program, the total chloride flux at concrete surfaces, q_{Cl} $(\frac{mol}{m2}.sec)$, is simulated with the diffusive component, q_{diff}, as introduced in equation (2-49). Due to lack of supplementary experimental documents, the effect of quasi-adsorption flux, q_{ads} on the total chloride flux at concrete surfaces is ignored.

5.2 Model description

The chloride analysis in this chapter is focused on the experimental tests conducted by Maruya et al. (1998) on prismatic concrete specimens which were made of Ordinary Portland Cement, OPC and subjected to different environmental conditions. Except the top concrete surface, other concrete surfaces were sealed by epoxy, so the chloride ions only diffused along the height of concrete specimens. As shown in Figure 5.2, the three-dimensional finite element model is a 5cm × 10cm × 5cm rectangular cube was simplified to two-dimensional finite element model, which consists of 22 nodes and 10 four-node quadrilateral (4Q) elements. According to the experimentally recorded chloride distribution along the height of concrete, the finer element size was adopted close to the top surface.

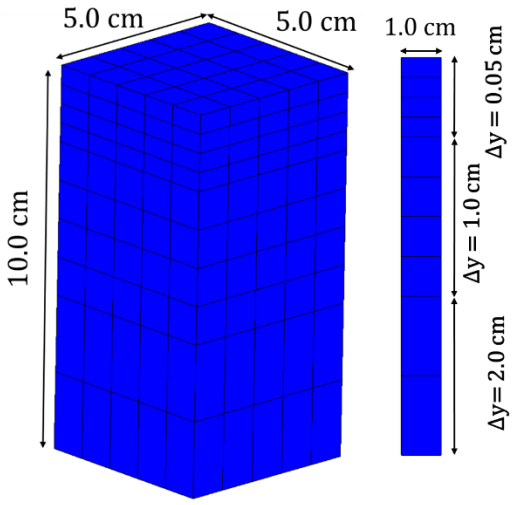

Figure 5.2: 3D finite element model in chloride diffusion analysis based on the concrete specimens in the experimental tests by Maruya et al. (1998)

Also, in accordance with the characteristics of concrete specimens in the experimental tests by Maruya et al. (1998), concrete density and water to cement ratio were set equal to 2300 Kg/m^3 and 0.5, respectively. The paste porosity was set to 0.28. More detailed about the concrete mixture is presented in Table 5.1. Based on the concrete mixture proportions and equation (5-5), $C_{f,factor}$ was set equal to 0.24805 in chloride diffusion analysis.

Table 5.1: Mixture proportion for the experimental tests by Maruya et al. (1998)

Mass of water per unit volume of concrete, $W_{bound\ water}$ (Kg/m^3)	175
Mass of binder per unit volume of concrete, W_{cement} (Kg/m^3)	350
Mass of sand per unit volume of concrete, $W_{fine\ aggregate}$ (Kg/m^3)	886

The time step of analysis was set to one day and the chloride concentration was initialized to zero. The concrete specimens in the experimental test were under the controlled temperature of 20°C and 100% relative humidity, so in this research, the coupling effects of thermal and moisture transport analysis were simplified to the constant uniform temperature and relative humidity distribution during time of analysis. All concrete surfaces except the top concrete surface were modeled as insulated boundaries. For 365 days, concrete specimens were immersed in the 3% NaCl solution by mass of water, where the chloride ion concentration is 529 mol/m^3. Since, the top concrete surface was continuously exposed to the constant chloride ion concentration, in the chloride analysis, the boundary condition at the top surface was simplified to the constant essential boundary condition (=529 mol/m^3).

5.3 Chloride diffusion analysis results and discussions

The time history of chloride concentration at different depths is presented in Figure 5.3. It can be seen that the chloride ions mainly accumulated in vicinity of top surface that was constantly immersed in a 3% NaCl. Due to the gradient of chloride ion concentration, chloride ions transported along the depth of concrete from the top surface with the highest chloride content to the bottom surface.

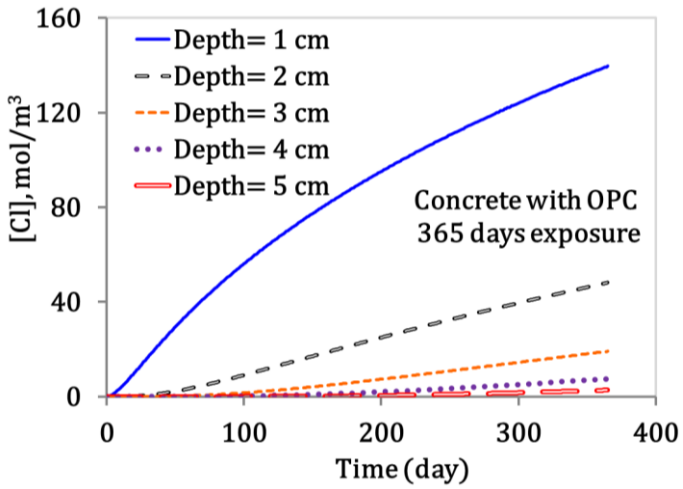

Figure 5.3: Time history of chloride concentration, [Cl], for the concrete model with geomentry and boundary conditions based on the experimental test by Maruya et al. (1998) with Ordinary Portland Cement (OPC) under constant exposure to 3% NaCl solution for 365 days

The comparison between the analytically obtained and experimentally recorded chloride concentration distribution, at a time of 365 days, is presented in Figure 5.4. It can be observed that the overall quantitative and qualitative trends of the analytically obtained chloride concentration are similar to the experimentally recorded. There is still a room to reduce the deviation from the experimental results by calibration of the input parameters based on more supplementary experimental documents.

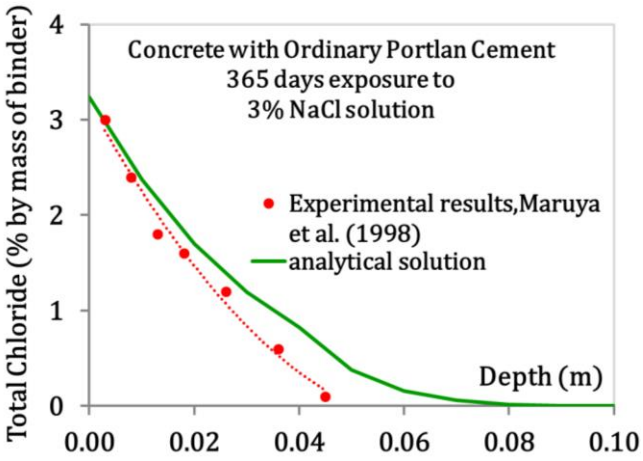

Figure 5.4: Comparison between the analytically obtained and experimentally recorded chloride concentration distribution for the concrete models based on the experimental tests by Maruya et el. (1998) at time of 365 days

5.4 Sensitivity analysis with the binding capacity

In Figure 5.5, the binding chloride, C_b is depicted as the nonlinear function of free chloride, C_f for concrete with Ordinary Portland Cement (OPC); Blast Furnace Slag (BFS) with 50% cement replacement; and Fly Ash (FA) with 40% cement replacement.

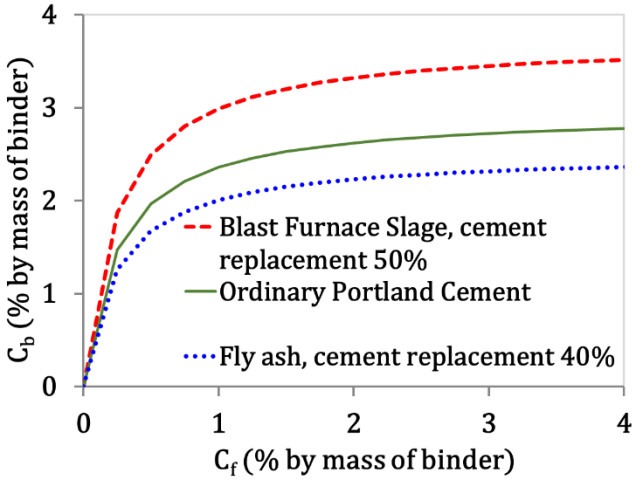

Figure 5.5: Binding chloride, Cb obtained by the nonlinear model proposed by Maekawa et al. (2009)

In the analysis program, the chloride concentration ions in pore liquid, [Cl], is defined as the output of the chloride diffusion analysis. The contribution of free chloride, C_f, to the total chloride content in concrete (% by mass of binder) is calculated by the equation (5-5), while in equation (5-3), the binding chloride is calculated as a nonlinear function of free chloride. Finally, total chloride content is determined as the summation of free chloride and binding chloride in concrete. In Figure 5.6, the analytically obtained total chloride content are illustrated for the concrete with OPC and BFS with 50% replacement.

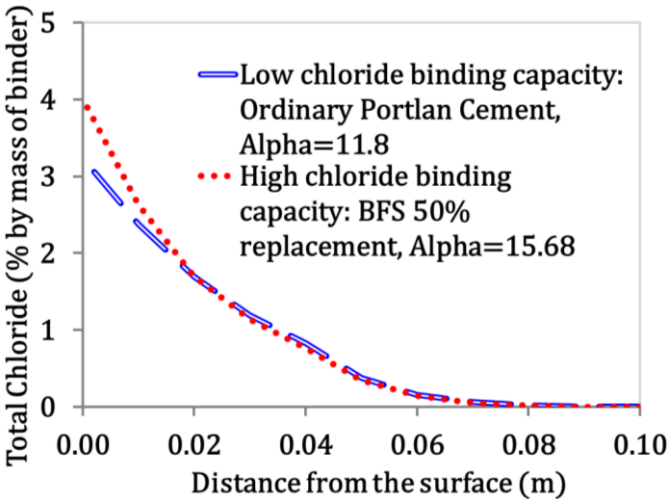

Figure 5.6: Effect of binding capacity on total chloride content in concrete for the concrete model based on the experimental tests by Maruya et al. (1998) under constant exposure to 3% NaCl solution for 365 dys

In accordance with the equation (5-4), the binding capacity parameter, α increases from 11.8 for the concrete with OPC to 15.68 for the concrete with BFS 50% replacement. By increasing the binding capacity, the contribution of binding chloride to total chloride content is elevated. However, as shown in Figure 5.1, the binding chlorides at concrete surfaces neutralize the positive electric charges of concrete pore wall structure. Therefore, the increase in binding chloride leads to reduction of quasi-adsorption flux at concrete

surfaces. In this research, the quasi-adsorption effect at concrete surfaces is ignored due to the lack of valid experimental data.

6 Methodology and analysis of coupled advection-diffusion of chemical substances in porous medium

Chemical substances such as chloride ions can transport in concrete as a porous medium due to the coupling effects of advection and diffusion. The analysis program is able to simulate the coupled advection-diffusion of chemical substances in 1D, 2D and 3D porous medium. If the advective effect is dominant, the pattern of chemical substances distribution in concrete is altered. In this research, the streamline-upwind Petrov-Galerkin (SUPG) has been implemented to address the spatial instabilities due to the huge advection effect.

6.1 Methodology of advection-diffusion analysis

In the analysis program, the advection velocity is defined as a function of the water flux vector, $\overrightarrow{\mathrm{Flux}_{\mathrm{Fluid}}}$. The time-dependent distribution of water flux vector at each Gaussian point is obtained by the moisture transport analysis. Equation (6-1) introduces the advection velocity vector, $\overrightarrow{V_{adv}}$ as a function of water content, θ_w, whereθ_w should be always greater than zero.

$$\overrightarrow{V_{adv}} = -\frac{\overrightarrow{\mathrm{Flux}_{\mathrm{Fluid}}}}{\theta_w} \tag{6-1}$$

In advance, the advection- diffusion coupling effect on the chloride transport in concrete is evaluated by the "Peclet number", P_e (Fish and Belytschko 2007), as follows:

$$P_e = \frac{V_{adv} h_{elem}}{2 D_{Cl,diff}} \tag{6-2}$$

where $D_{Cl,diff}$ is the chloride diffusion coefficient and h_{elem} is the element size. As defined in equation (6-3), the element size is equal to the length of truss bar element, while it is equal to the second and third root of domain size for four-node quadrilateral (Q4) and eight-node hexahedral (H8) elements, respectively.

$$h_{elem} = \begin{cases} L^{(e)} & \text{One Dimentional} \\ \sqrt[2]{A^{(e)}} & \text{Two Dimensional} \\ \sqrt[3]{V^{(e)}} & \text{Three Dimensional} \end{cases} \tag{6-3}$$

Peclet number is referred as the ratio of advection to diffusion contribution to the ion transport along a specific direction. Due to high water velocity in concrete, the advective force may dominate the diffusive force. In accordance with Donea and Huerta (2003) and Fish and Belytschko (2007), if the Peclet number exceeds unity, the dominant advective force causes spatial instabilities in the chloride distribution in concrete medium. In the analysis program, the SUPG method and the stabilized SUPG method are implemented to simulate the coupling advection effect and also reduce the spatial instabilities due to the significant water velocity. Two integer parameters including iadvection and iSUPG are introduced in the analysis program to model the advection effect and stabilize the chloride distribution. The iadvection and iSUPG parameters are initialized to unity in the coupled advection-diffusion analysis, when SUPG method is used to reduce the spatial instabilities.

In multi-dimensional analysis, the advection velocity and the Peclet number are calculated in each direction. As shown in Figure 6.1, $\overrightarrow{e_\xi}$ and $\overrightarrow{e_\eta}$ are the unit vectors, while h_ξ and h_η are the element lengths along ξ and η directions.

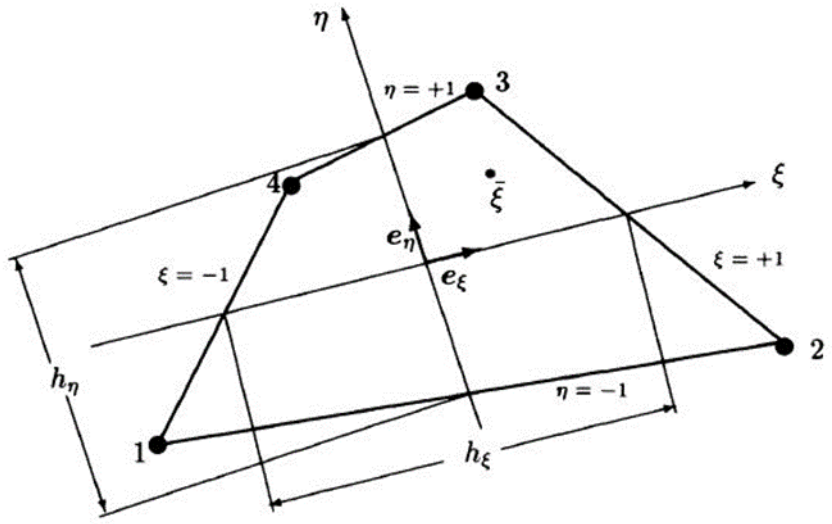

Figure 6.1: Schematic illustration of a Q4 element with parametric coordinates and basis vectors shown (Donea and Huerta, 2003)

Donea and Huerta (2003) proposed the numerical equations to calculate the unit vectors, $\overrightarrow{e_\xi}$ and $\overrightarrow{e_\eta}$ and the element lengths along the unit vectors, h_ξ and h_η , as follows:

$$\begin{cases} \overrightarrow{e_\xi} = \dfrac{1}{\mathrm{norm}(\overrightarrow{e_\xi})} \begin{Bmatrix} \dfrac{\partial x}{\partial \xi} \\ \dfrac{\partial y}{\partial \xi} \end{Bmatrix}_{\substack{\xi=0.0 \\ \eta=0.0}} \\ \overrightarrow{e_\eta} = \dfrac{1}{\mathrm{norm}(\overrightarrow{e_\eta})} \begin{Bmatrix} \dfrac{\partial x}{\partial \eta} \\ \dfrac{\partial y}{\partial \eta} \end{Bmatrix}_{\substack{\xi=0.0 \\ \eta=0.0}} \end{cases} \tag{6-4}$$

$$\begin{cases} \{x_{11}\} = \begin{Bmatrix} x(\xi = -1.0, \eta = 0.0) \\ y(\xi = -1.0, \eta = 0.0) \end{Bmatrix}, \{x_{21}\} = \begin{Bmatrix} x(\xi = 1.0, \eta = 0.0) \\ y(\xi = 1.0, \eta = 0.0) \end{Bmatrix} \\ \{x_{12}\} = \begin{Bmatrix} x(\xi = 0.0, \eta = -1.0) \\ y(\xi = 0.0, \eta = -1.0) \end{Bmatrix}, \{x_{22}\} = \begin{Bmatrix} x(\xi = 0.0, \eta = 1.0) \\ y(\xi = 0.0, \eta = 1.0) \end{Bmatrix} \end{cases} \quad (6\text{-}5)$$

$$\begin{cases} \overrightarrow{r_1} = \{x_{21}\} - \{x_{11}\} \\ \overrightarrow{r_2} = \{x_{22}\} - \{x_{12}\} \end{cases} \quad (6\text{-}6)$$

$$\begin{cases} h_\xi = \|\overrightarrow{r_1}\| \\ h_\eta = \|\overrightarrow{r_2}\| \end{cases} \quad (6\text{-}7)$$

Also, the components of the advection velocity, $V_{adv,\xi}$ and $V_{adv,\eta}$ in ξ and η directions, respectively, are calculated by the equation (6-8):

$$\begin{cases} V_{adv,\xi} = \overrightarrow{V_{adv}}.\overrightarrow{e_\xi} \\ V_{adv,\eta} = \overrightarrow{V_{adv}}.\overrightarrow{e_\eta} \end{cases} \quad (6\text{-}8)$$

Now, the Peclet number in different directions, $P_{e,\xi}$ and $P_{e,\eta}$ are determined by the equation (6-9):

$$\begin{cases} P_{e,\xi} = \frac{V_{adv,\xi}.h_\xi}{2D_{Cl,diff}} \\ P_{e,\eta} = \frac{V_{adv,\eta}.h_\eta}{2D_{Cl,diff}} \end{cases} \quad (6\text{-}9)$$

As shown in equation (6-10), Donea and Huerta (2003) introduced $\bar{\xi}$ and $\bar{\eta}$ as the critical parameters to control the spatial instabilities in the distribution of chemical substances.

$$\begin{cases} \bar{\xi} = \mathrm{Coth}P_{e,\xi} - 1/P_{e,\xi} \\ \bar{\eta} = \mathrm{Coth}P_{e,\eta} - 1/P_{e,\eta} \end{cases} \tag{6-10}$$

Also, Donea and Huerta (2003) proposed the numerical formula to calculate the scalar artificial diffusion coefficient, $\bar{V}$, as follows:

$$\bar{V} = \frac{(\bar{\xi}.V_{adv,\xi}.h_{\xi} + \bar{\eta}.V_{adv,\eta}.h_{\eta})}{2} \tag{6-11}$$

As shown in equation (6-12), Donea and Huerta (2003) defined the stabilization parameter, τ as a scalar function of the Peclet number, the element size, the advection velocity and the direction. The parameter τ is applied to reduce the spatial instabilities due to the huge water velocity.

$$\tau = \frac{\bar{V}}{\|\overrightarrow{V_{adv}}\|^2} \tag{6-12}$$

$\{r_v\}$ vector is introduced by Donea and Huerta (2003) to model the least square part of an element matrix which is symmetric, as follows:

$$\{r_v\} = \{V_{adv,x} \quad V_{adv,y}\} \begin{bmatrix} \frac{\partial N_1^{(e)}}{\partial x} & \frac{\partial N_2^{(e)}}{\partial x} & \frac{\partial N_3^{(e)}}{\partial x} & \frac{\partial N_4^{(e)}}{\partial x} \\ \frac{\partial N_1^{(e)}}{\partial y} & \frac{\partial N_2^{(e)}}{\partial y} & \frac{\partial N_3^{(e)}}{\partial y} & \frac{\partial N_4^{(e)}}{\partial y} \end{bmatrix} \tag{6-13}$$

where $V_{adv,x}$ and $V_{adv,y}$ are the components of the advection velocity along the x and y axis, respectively: In equation (6-14), the stabilization parameter, r_{vC} is the dot product of the advective term, $\{r_v\}$, and the chloride concentration, $\{C_{Cl}\}$, at each element.

$$r_{vC} = \sum_{j=1}^{4} r_v(j).C_{Cl}^{(e)}(j) \quad (6\text{-}14)$$

For the iadvection and iSUPG of unity, the stabilized finite element method is implemented in advection-diffusion equation analysis. The contribution of advection to the element coefficient array, $\left[k^{(e)}\right]_{(advection)}$, and the element equivalent right hand-side vector, $\left\{f^{(e)}\right\}_{(advection)}$ are calculated using the following equations:

$$\left[k^{(e)}\right]_{(advcetion)} = \int\int\int_{\Omega} \tau.\{r_v\}^T.\{r_v\}d\forall \quad (6\text{-}15)$$

$$\left\{f^{(e)}\right\}_{(advection)} = \int\int_{\Gamma} (\tau.\{r_v\}.r_{vC} - \{r_v\}.S(x,y,z,t)d\Gamma \quad (6\text{-}16)$$

where $S(x,y,z,t)$ is the time-dependent chloride supply in the chloride diffusion analysis. Finally, the element coefficient array, $\left[k^{(e)}\right]$, and the element equivalent right hand-side vector, $\left\{f^{(e)}\right\}$ are determined by the following equations:

$$\left[k^{(e)}\right] = \left[k^{(e)}\right]_{(diffusion)} + \left[k^{(e)}\right]_{(advcetion)} \quad (6\text{-}17)$$

$$\left\{f^{(e)}\right\} = \left\{f^{(e)}\right\}_{(diffusion)} + \left\{f^{(e)}\right\}_{(diffusion)} \quad (6\text{-}18)$$

where $\left[k^{(e)}\right]_{(diffusion)}$ and $\left\{f^{(e)}\right\}_{(diffusion)}$ are the element coefficient array and the element equivalent right hand-side vector in chloride diffusion analysis which are determined by equations (2-17) and (2-18), respectively.

6.2 Model description

In this thesis, the coupled advection-diffusion of chemical substance in concrete was evaluated for 1D, 2D and 3D finite element models. The element size is equal to 1.0 m. As shown in Figure 6.2, the water flows only along the longitudinal direction of the concrete model. Also, due to the gradient of chloride concentration, chloride ions diffuse along the length.

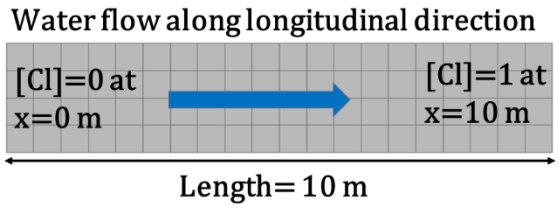

Figure 6.2: Schematic illustration of 2D finite element model and boundary conditions in advection-diffusion problem

For 1D, 2D and 3D models, the contribution of advective force to chloride transport was evaluated in two different cases. In the first case, the Peclet number was set equal to 0.1, while in the second case, the Peclet number is significantly increased to the huge value of 3.0.

6.3 Analysis results and discussions

Figures 6.3 represents the chloride distribution in 1D, 2D and 3D models, when Pe is equal to 0.1. When Pe is less than unity, diffusion is the dominant force to lead the chloride transport in concrete. As shown in Figure 6.3, since the chloride distribution along the length has no spatial instability due to the advective force, the stabilized SUPG method has no significant effect on the chloride concentration along the length of concrete.

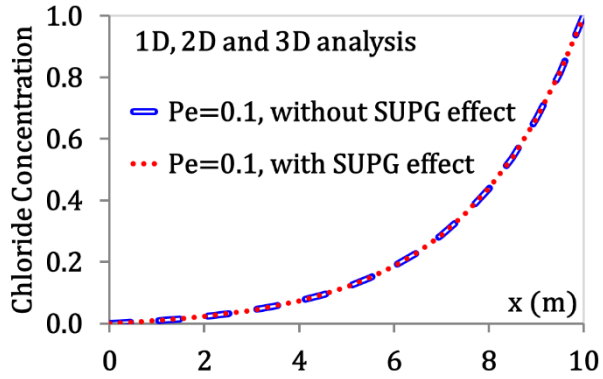

Figure 6.3: Chloride concentration distribution along the length of concrete in diffusive dominnt chloride transporat (Pe=0.1)

By increasing the Peclet number from 0.1 to 3.0, chloride transport is significantly impacted by the advective force. As shown in Figures 6.4 and 6.5, the spatial instabilities due to the dominant advective force is addressed by using the SUPG method. Compare to 1D analysis, the SUPG method works better in multidimensional analysis.

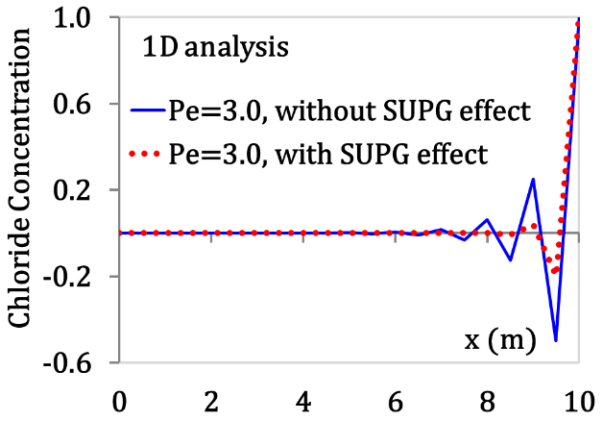

Figure 6.4: Chloride concentration distribution along the length of concrete in 1D advective dominnt chloride transporat (Pe=3.0)

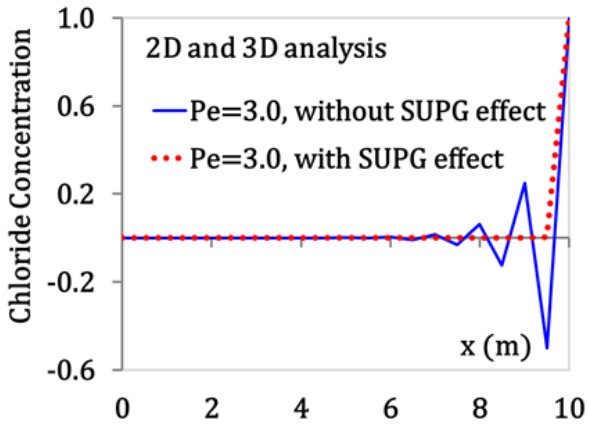

Figure 6.5: Chloride concentration distribution along the length of concrete in 2D and 3D advective dominnt transporation (Pe=3.0)

6.3.1 Effect of crack

In this research, the crack openings in concrete are simulated as the idealized diffusion channels with less tortuosity, compare to the pore channels. Therefore, Chloride ions can easily diffuse through the cracked opening. In accordance with the equations (2-42) and (2-43), the chloride diffusion coefficient rises when the concrete crack width increases. On the other hand, the advective transport of chloride depends on the water velocity in concrete. Since concrete porosity is the constant parameter which is not affected by crack propagation in concrete, the moisture transport analysis and so water velocity would not influenced by crack propagation. Consequentially, the increase in chloride diffusion coefficient results in the reduction of the Peclet number. Modeling of moisture transport in cracked concrete is recommended as the future studies.

6.3.2 Effect of mesh size

According to the equation (6-2), the Peclet number is reduced due to the mesh refinement. Therefore, the contribution of advective force to chloride transport is reduced and so, the spatial instabilities due to the dominant advective transport is decreased as well. Consequently, mesh refinement facilitates the convergence of the advection-diffusion analysis. However, in fluid analysis, mesh refinement may end to different consequence. Generally, the element size in fluid problems should be defined based on optimization. For example, by reducing the element size of the concrete bridge piers which is exposed to the turbulent water flow during the service life, the small elements of concrete piers in vicinity of sea water may experience the huge water gradient. Therefore, mesh refinement may increase the advective velocity at the interface of concrete piers and sea water.

7 Conclusions

This thesis contributed a nonlinear finite element analysis program called *VT-MultiPhys*, to enable multi-physics simulations of chloride-induced corrosion in concrete structures. The present study has proposed the modeling scheme adopted for heat conduction, moisture transport, chemical diffusion, together with preliminary verification and validation analyses. The main conclusions of this study are as follows.

- The created program can provide time-histories of key state variables, such as temperature, moisture content and concentration of chemical agents such as chloride ions, which can initiate corrosion.
- Finite element analyses have been shown capable of satisfactorily reproducing the moisture distributions from experimental tests. This is not the case for temperature distributions. The reason for the discrepancy between analytically obtained and experimentally recorded temperature distributions has not been established.
- A limited set of validation analysis for chloride transport has given satisfactory agreement with experimentally obtained chloride content distributions.
- Sensitivity analyses conducted for moisture transport and chloride diffusion have demonstrated the impact of various parameters in the employed constitutive laws.

The capability of the Streamline Upwind Petrov-Galerkin (SUPG) scheme to eliminate spurious spatial oscillations in the concentration fields has been verified for cases where advection dominates the transport of chemical species.

7.1 Recommendations for Future Work

A major part of this thesis was dedicated to the actual programming of *VT-MultiPhys*. This is why the amount of validation analyses for various physico-chemical processes in concrete was rather limited. With the simulation code completed, future studies can proceed to investigate several key topics identified in this study.

First of all, it is necessary to further investigate and validate the analysis scheme for heat conduction. The analyses presented herein considered experimental tests conducted by a single research group. Given the discrepancy between analysis and experiment, along with the verification that computational simulation can reproduce the results of closed-form solutions for simple cases, it is necessary to determine the reason for the disagreement between analytically obtained and experimentally recorded temperature distributions, as well as conduct further validation analyses, preferably using data from experiments conducted by different research groups.

Second, fully coupled analyses on bridge girder geometries are necessary, to investigate the anticipated impact of chloride transport on corrosion propensity, and determine the sensitivity of the analytical results on various parameters of the environment (e.g., relative humidity, temperature) and of the concrete material (e.g., porosity).

Besides the above, future research with *VT-MultiPhys* will need to also consider the actual evolution of corrosion for cases where the chloride content exceeds the critical value corresponding to corrosion initiation. This will allow the determination of the evolution of sectional loss in reinforcing bars and/or prestressing strands, as well as the estimation of the instant where visible damage (i.e., corrosion-induced cracking) is to be expected. Obviously, such simulations will allow the consideration of mechanical deformation, by means of appropriate constitutive laws providing the stresses as functions of the strains. The occurrence of cracking will in turn accelerate the progress of corrosion. Quantifying the extent of such cracking-induced corrosion acceleration must also be investigated in future studies.

Finally, this study has been focused on chloride-induced corrosion. The element formulations and solution algorithms in *VT-MultiPhys* also allow the investigation of other long-term deterioration mechanisms, such as carbonation-induced corrosion, alkali-silika reaction (ASR) and sulfate attack. The present contribution will hopefully enable and facilitate future research in these topics, through the formulation and implementation of proper constitutive laws and chemical reaction equations.

References

1. Alhozaimy, A., Hussain, R. R., Al-Zaid, R., and Al-Negheimish, A. (2012) "Coupled effect of ambient high relative humidity and varying temperature marine environment on corrosion of reinforced concrete." Constr. Build. Mater, Vol. 28, No. 1, pp. 670–679.
2. Bazant, Z.P. (1979) "Physical Model for Steel Corrosion in Concrete Sea Structures—Application." ASCE J Struct Div, V. 105, No. 6.
3. Bentur, A., Diamond, S., and Berke, N. S. (1997) "Steel corrosion in concrete." E and FN Spon, New York, 78 pp.
4. Broomfield, J.P. (2007) "Corrosion of Steel in Concrete- Understanding, investigation and repair." Taylor & Francis, New York, 294 99.
5. Care, S. (2003) "Influence of aggregates on chloride diffusion coefficient into mortar." Cement and Concrete Research 33 (2003) 1021–1028.
6. McCarter, W. J., and Garvin, S. (1989). "Dependence of electrical impedance of cement-based materials on their moisture condition." J. Phys. D: Appl. Phys., 22(11), 1773–1776.
7. Castel, A., Francois, R., and Arliguie, G. (2000) "Mechanical behavior of corroded reinforced concrete beams—Part 1: Experimental study of corroded beams." Mater. Struct, 33(9), 539–544.
8. Christensen, R.M. (1979) "Mechanics of Composite Materials." Wiley Interscience, New York.
9. Collepardi, M., Marcialis, A., and Turriziani, R. (1972), "Penetration of chloride Ions into Cement Pastes and Concretes." Journal of the American Ceramic Society-Discussions and Notes Vol. 55, No. 10.
10. Dao, L., Dao, V., Kim, S., and Ann, K. Y. (2010a) "Modeling Steel Corrosion in Concrete Structures - Part 1: A New Inverse Relation between Current Density

and Potential for the Cathodic Reaction." Int. J. Electrochem. Sci., 5 (2010) 302 – 313

11. Dao, L., Dao, V., Kim, S., and Ann, K. Y. (2010b) "Modeling Steel Corrosion in Concrete Structures - Part 2: A Unified Adaptive Finite Element Model for Simulation of Steel Corrosion." Int. J. Electrochem. Sci., 5 (2010) 314 – 326.
12. Das, B. B., Singh, D. N., and Pandey, S. P. (2012) "Rapid chloride ion permeability of OPC- and PPC-based carbonated concrete." J. Mater. Civ. Eng.,10.1061/(ASCE)MT.1943-5533.0000415, pp. 606–611.
13. Donea, J., and Huerta, A. (2003) "Finite Element Methods for Flow Problems." John Wiley & Sons, Ltd, ISBN: 0-471-49666-9.
14. Du, Q. (2016) "Finite Element Modelling of Steel/Concrete Bond for Corroded Reinforcement." M.A.Sc. Thesis, University of Ottawa, Ottawa, Canada, 151 pp.
15. Elbadry, M., and Ghali, A. (1983) "Temperature Variations in Concrete Bridges." Journal of Structural Engineering, V. 109, No. 10, pp. 2355- 2374.
16. Emerson, M. (1973) "The Calculation of the Distribution of Temperature in Bridges." TRRL Report LR561, Department of the Environment, Crowtowne, England.
17. Farzampour, A., and Radlinska, A. (2016) "The effect of temperature and humidity on strength development of grouts." International concrete sustainability conference, Washington D.C.
18. Farzampour, A. (2017) "Temperature and humidity effects on behavior of grouts." Advances in concrete construction, An international journal, Vol. 5, Issue 6, pp.659-669.
19. Fish, J., and Belytschko, T. (2007) "A First Course in Finite Elements." John Wiley & Sons, Inc., New Jersey, 344 pp.
20. Garboczi, E.J., and Bentz, D.P. (1992) "Computer Simulation of the Diffusion coefficient of Cement Based Materials." Journal of Material Sciences, Vol. 27, pp. 2083-2092.

21. Ghods, P., Isgor, O.B., and Pour-Ghaz M. (2008) “Experimental verification and application of a practical corrosion model for uniformly depassivated steel in concrete.” Materials and Structures, Vol. 41, pp. 1211– 1223.
22. Glass, G.K., and Buenfeld, N.R. (2000) “The influence of chloride binding on the chloride-induced corrosion risk in reinforced concrete.” Corrosion Science, Vol. 42, pp. 329- 344.
23. Gouda, V. K. (1970) “Corrosion and Corrosion Inhibition of Reinforcing Steel: I. Immersed in Alkaline Solutions.” British Corrosion Journal, V. 5, No. 5.
24. Hansen, E.J., and Saouma, V.E. (1999a) “Numerical Simulation of Reinforced Concrete Deterioration—Part I: Chloride Diffusion.” ACI Materials Journal, V. 96, No. 2.
25. Hansen, E.J., and Saouma, V.E. (1999b) “Numerical Simulation of Reinforced Concrete Deterioration: Part II—Steel Corrosion and Concrete Cracking.” ACI Materials Journal, V. 96, No. 3.
26. Hall, Ch., and D.Hoff, W. (2012) “Water transport in Brick, Stone and Concrete.” Spon Press, New York, US, second edition, 370 pp.
27. Huang, Q., Jiang, Zh., Gu, X., Zhang, W., and Guo, B. (2015) “Numerical simulation of moisture transport in concrete based on a pore size distribution model.” Cement and Concrete Research 67 (2015) 31–43.
28. Isgor, O.B., and Ghani Razaqpur, A. (2004) “Finite element modeling of coupled heat transfer, moisture transport and carbonation processes in concrete structures.” Cement & Concrete Composites 26 (2004) 57–73.
29. Isgor, O.B., and Ghani Razaqpur, A. (2006) “Modelling steel corrosion in concrete structures.” Materials and Structures (2006) 39:291–302.
30. Jang, S.Y., Kim, B.S., and Oh, B.H (2011) “Effect of crack width on chloride diffusion coefficients of concrete by steady-state migration tests.” Cement and Concrete Research, Vol. 41, No. 1, pp. 9- 19.

31. Ji, G. (2006) “On the Numerical Solution of Laplace’s Equation with Nonlinear Boundary Conditions for Corrosion of Steel in Concrete.” M.A.Sc. Thesis, Carleton University, Ottawa, Ontario, Canada.
32. Koutromanos, I., (2018) “Fundamentals of finite element analysis- Linear finite element analysis.” John Wiley & Sons Inc., New Jersey, 710 pp.
33. Kulakowski, M. P., Pereira, F. M., Molin, D. (2009) “Carbonation-induced reinforcement corrosion in silica fume concrete.” Construction and Building Materials, Vol. 23, No. 3, pp. 1189–1195.
34. Li, Ch. Q. (2002) “Initiation of Chloride-Induced Reinforcement Corrosion in Concrete Structural Members-Prediction.” ACI Structural Journal. V. 99. No. 2, Title no. 99614.
35. Li, G., Hu, F., and Wu, Y. (2011) “Chloride ion penetration in stressed concrete.” J. Mater. Civ. Eng., 10.1061/(ASCE)MT.1943-5533 .0000281, pp. 1145–1153.
36. Lienemann, J., Youse, A., and Korvink, J.G. (2005) “Nonlinear heat transfer modelling.” Report, University of Freiburg, Germany.
37. Luo, R., Cai, Y., Wang, Ch., and Huang, X. (2003) “Study of chloride binding and diffusion in GGBS concrete.” Cement and Concrete Research 33 (2003) 1 –7.
38. Luping, T., and Gulikers, J. (2007) "On the mathematics of time-dependent apparent chloride diffusion coefficient in concrete." Cement and Concrete Research. Vol. 37, No. 4, pp. 589–595.
39. Maekawa, K., Chaube, R., and Kishi, T. (1999) “Modeling of Concrete Performance, Hydration, Microstructure Formation and Mass Transport.” E& FN Spon, London.
40. Maekawa, K., Ishida, T., and Kishi, T. (2009) “Multi- scale modeling of structural concrete.” Taylor and Francis, New York, 665 pp.
41. Maekawa, K., Kishi, T., and Ishida, T. (2003) “Multi- scale modeling of concrete performance: integrated material and structural mechanics.” Journal of advanced concrete technology. Vol.1, No. 12. Pp. 91-126.

42. Mangat, P., and Molloy, B. (1994) “Prediction of Long-Term Chloride Concentration in Concrete.” Materials and Structures, V. 27, No. 170, pp. 338-346.
43. Marques, P. F., and Costa, A. (2010) “Service life of RC structures: Carbonation induced corrosion. Prescriptive vs. performance- based methodologies” Construction and Building Materials 24 (2010) 258–265.
44. Martin-Perez, B. (1999) “Service Life Modeling of R.C. Highway Structures Exposed to Chlorides.” Ph.D. Thesis, University of Toronto, Canada, 168pp.
45. Martin-Perez, B., Pantazopoulou, S.J., Thomas, M.D.A. (2001) “Numerical solution of mass transport equations in concrete structures.” Computers and Structures. Vol. 79, pp. 1251-1264.
46. Maruya, T. (1995), “Development of a method of a analyzing the movement of Chloride ions in concrete.” Ph.D. thesis, the university of Tokyo.
47. Maruya, T., Tangtermsirikul, S., and Matsuoka, Y. (1998), “Modeling of chloride ion movement in the surface layer of hardened concrete.” JSCE NO. 585/ V-38.
48. Michel, A., Geiker, M.R., Olesen, J.F., and Stang, H. (2013) “Reinforcement Corrosion: Numerical Simulation and Service Life Prediction”. Kgs. Lyngby: Technical University of Denmark (DTU). (B Y G D T U. Rapport).
49. McCarter, W. J., and Garvin, S. (1989). “Dependence of electrical impedance of cement-based materials on their moisture condition.” J. Phys. D: Appl. Phys., 22(11), 1773–1776.
50. Millard, S. G., Law, D., Bungey, J. H., and Carins, J. (2001) “Environmental influences on linear polarization corrosion rate measurement in reinforced concrete.” NDT& International 34 (2001) 409-417.
51. Mindess, S., Young, J.F., and Darwin, D. (2002) “Concrete.” Second ed. Prentice Hall, Englewood, Cliffs, NJ.
52. Mingzhong, ZH., and Guang, Y. (2010) “Modelling of Time Dependency of Chloride Diffusion Coefficient in Cement Paste.” Journal of Wuhan University of Technology-Mater. Sci. Ed., DOI 10.1007/s11595-010-0071-6.

53. Miyazato, Sh., and Otsuki, N. (2010) “Steel Corrosion Induced by Chloride or Carbonation in Mortar with Bending Cracks or Joints.” Journal of Advanced Concrete Technology Vol. 8, No. 2, 135-144.
54. Mokarem, D. W., (2017) “Portland Cement, CEE 4614: Advanced Structural Concretes”, Department of civil and environmental engineering, Virginia Polytechnic Institute and State University.
55. Montemor, M. F., Simões, A. M. P., and Ferreira, M. G. S. (2003) “Chloride-induced corrosion on reinforcing steel: From the fundamentals to the monitoring techniques.” Cem. Concr. Compos, Vol. 25, pp. 491– 502.
56. Moreno, M., Morris, W., Alvarez, M.G., and Duff, G.S. (2004) “Corrosion of reinforcing steel in simulated concrete pore solutions Effect of carbonation and chloride content.” Corrosion Science, V. 46, 2681–2699.
57. Moser, R., Holland, B., Kahn, L., Singh, P., and Kurtis, K. (2011) “Durability of Precast Prestressed Concrete Piles in Marine Environment: Reinforcement Corrosion and Mitigation – Part 1.” Office of Materials and Research Georgia Department of Transportation, School of civil and environmental engineering, Georgia Institute of Technology.
58. Munn, R.S., and Devereux, O. F. (1991) “Numerical Modeling and Solution of Galvanic Corrosion Systems: Part I. Governing Differential Equation and Electrodic Boundary Conditions, CORROSION.” Vol. 47, No. 8, pp. 612-618.
59. Na, O., Cai, X.Ch., and Xi, Y. (2017), “Corrosion Prediction with Parallel Finite Element Modeling for Coupled Hygro-Chemo Transport into Concrete under Chloride-Rich Environment.” Materials, Vol. 10, No. 350.
60. Papadakis, V.G., Vayenas, C.G., and Fardis, M.N. (1991) “Physical and chemical characteristics affecting the durability of concrete.” ACI materials journal, Vol.88, No.2.
61. Potgieter, I.C., and Gamble, W. (1983) “Response of Highway Bridges to Nonlinear Temperature Distributions.” Structural Engineering Series No. 505, Report No. HWA/IL/UI-201, 291pp.

62. Pour-Ghaz, M. (2007) “A Novel Approach for Practical Modelling of Steel Corrosion in Concrete.” M.A.Sc. Thesis, Carleton U niversity, Ottawa, Ontario, Canada.
63. Pour-Ghaz, M., Isgor, O.B., and Ghods, P. (2009- a) “Quantitative Interpretation of Half-Cell Potential Measurements in Concrete Structures.” Journal of Materials in Civil Engineering, Vol. 21, No. 9, ASCE, ISSN 0899-1561/2009/9-467–475.
64. Pour-Ghaz, M., Isgor, O.B., and Ghods, P. (2009- b) “The effect of temperature on the corrosion of steel in concrete. Part 2: Model verification and parametric study.” Corrosion Science 51 (2009) 426–433.
65. Priestley, MJN. (1976) “Linear heat-flow analysis of concrete bridge decks.” Research Reports 76/3, Department of Civil Engineering, University of Canterbury, Christchurch.
66. Saetta, A. V., and Vitaliani, R. V. (2004) “Experimental investigation and numerical modeling of carbonation process in reinforced concrete structures Part I: Theoretical formulation.” Cement and Concrete Research 34 (2004) 571–579.
67. Saetta, A.V, Scotta, R., and Vitaliani, R.V. (1993) “Analysis of Chloride Diffusion into Partially Saturated Concrete.” ACI Materials Journal, V. 90, No. 5, pp. 441-451.
68. Samson, E., and Marchand, J. (2003) “Calculation of ionic diffusion coefficients on the basis of migration test result.” Materials and Structures / Matériaux et Constructions, Vol. 36, No. 257, 156-165.
69. Shin, K.Y., Kim, S.B., Kim, J.H., Chung, M., and Jung, P.S. (2002) “Thermo-physical Properties and Transient Heat Transfer of Concrete at Elevated Temperatures.” Nuclear Engineering and Design, Vol. 212, No. 2, pp. 233- 241.
70. Silva, N. (2013) “Chloride Induced Corrosion of Reinforcement Steel in Concrete; Threshold Values and Ion Distributions at the Concrete-Steel Interface.” Thesis for the degree of doctor of philosophy, Department of Civil and Environmental Engineering, Chalmers University of Technology, Gothenburg, Sweden, 66 pp.

71. Stern, M., and Geary, A.L. (1957) “Electrochemical Polarization- I. A Theoretical Analysis of the Shape of Polarization Curves.” Journal of the electrochemical society, Vol. 104, No. 1.
72. Tang, L., and Nilsson, L. (1994) “A Numerical Method for Prediction of Chloride Penetration into Concrete Structures.” The Modeling of Microstructure and its Potential for Studying Transport Properties and Durability, Saint-Rémy-lés-Chevreuse, France.
73. Therkeld, J.L. (1970) “Thermal environmental engineering.” Prentice-Hall, New Jersey, second edition.
74. Thomas, M., and Bamforth, Ph. (1999) “Modelling chloride diffusion in concrete Effect of fly ash and slag.” Cement and Concrete Research 29 (1999) 487–49.
75. Tuutti, K. (1982) “Corrosion of steel in concrete.” Swedish Cement and Concrete Research Institute, Stockholm.
76. Uhlig, H.H., and Revie, R.W. (1985) “Corrosion and corrosion control.” (3rd edn), Wiley-Interscience, New York, 1985. No. of pages: 458.
77. Van Genuchten, M.Th. (1980) "A closed-form equation for predicting the hydraulic conductivity of unsaturated soils." Soil Science Society of America Journal. Vol. 44, No. 5, pp. 892–898.
78. Wang, Y., and Xi, Y. (2017) “The Effect of Temperature on Moisture Transport in Concrete.” Materials, Vol. 10, No. 8, 926; doi: 10.3390/ma10080926.
79. Wong, H. S., Zhao, Y. X., Karimi, A. R., Buenfeld, N. R., and Jin, W.L. (2010) “On the penetration of corrosion products from reinforcing steel into concrete due to chloride-induced corrosion.” Corrosion Science, Vol. 52, pp. 2469–2480.
80. Xi, Y., and Bazant, Z.P. (1999) “Modeling Chloride Penetration in Saturated Concrete.” Journal of Materials in Civil Engineering, Vol. 11, No. 1, pp. 58- 65.
81. Xi, Y., Bazant, Z.P., and Jennings, H.M. (1994) “Moisture Diffusion in Cementitious Materials- Adsorption Isotherms.” Advanced Cement Based Materials, Vol. 1, No. 6, 248- 257.

82. Ye, Ch. Q., Hu, R. G., Dong, Sh. G., Zhang, X. J., Hou, R. Q., Du, R. G., Lin, Ch. J., and Pan, J. Sh. (2013) "EIS analysis on chloride-induced corrosion behavior of reinforcement steel in simulated carbonated concrete pore solutions." Journal of Electroanalytical Chemistry 688 (2013) 275–281.
83. Yoon, I.-S., Copuroglu, O., and Park, K.-B. (2007). "Effect of global climatic change on carbonation progress of concrete." Atmos. Environ., 41(34), 7274–7285.
84. Zheng, J.J., Zhou, X.Z., and Wu, Z.M. (2010) "A Simple Method for Predicting the Chloride Diffusion coefficient of Cement Paste." Materials and Structures, Vol. 43, No. 1, pp. 99-106.
85. Zhou, Ch.E. (2004) "Nonlinear Finite Element Analysis of Reinforced Concrete Structures." M.A.Sc. Thesis, University of Toronto, Toronto, Canada.
86. Zhou, Y., Gencturk, B., Willam, K., and Attar, A. (2015) "Carbonation-Induced and Chloride-Induced Corrosion in Reinforced Concrete Structures." Journal of Materials in Civil Engineering, ASCE, ISSN 0899-1561/04014245(17).
87. Corrosion of Embedded Metals, Retrieved from (2017 Portland Cement Association, PCA, www.cement.org)
88. Identifying And Treating Corrosion in Reinforced Concrete Structures, Retrieved from (04/02/2017 Concrete Preservation Technologies, cpt, https://cp-tech.co.uk)
89. New methodology predicts onset, progression of corrosion of reinforced concrete, Retrieved from (02/25/2014 NACE INTERNATIONAL, www.nace.org)
90. Service-Life Prediction for Reinforced Concrete Exposed to Chloride-Induced Corrosion Risk: Are we Just Rolling the Dice?, Retrieved from (02/21/2018 Giatech, https://www.giatecscientific.com)